Energy Storage Materials 66 (2024) 103240

Contents lists available at ScienceDirect

Energy Storage Materials

journal homepage: www.elsevier.com/locate/ensm

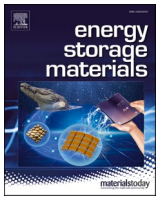

Three birds with one arrow: Multifunctional single-atom catalysts enable efficient lithium-sulfur batteries

Dawei Yang [a,b,1], Canhuang Li [b,1], Meenu Sharma [b], Mengyao Li [b,c], Jiaao Wang [e], Jishi Wei [d,*], Kun Liu [f], Yizhou Zhang [g,*], Junshan Li [h], Graeme Henkelman [e], Qiaobao Zhang [i,*], Andreu Cabot [b,j,**]

[a] Henan Province Key Laboratory of Photovoltaic Materials, School of Future Technology, Henan University, Kaifeng 475004, China
[b] Catalonia Institute for Energy Research - IREC, Sant Adrià de Besòs, Barcelona 08930, Spain
[c] School of Physics and Microelectronics, Zhengzhou University, Zhengzhou 450052, China
[d] College of Chemistry and Molecular Sciences, Henan University, Kaifeng 475004, China
[e] Department of Chemistry and the Oden Institute for Computational Engineering and Sciences, The University of Texas at Austin, Austin, TX 78712, USA
[f] Institute of Materials and Technology, Dalian Maritime University, Dalian 116026, China
[g] Institute of Advanced Materials and Flexible Electronics (IAMFE), School of Chemistry and Materials Science, Nanjing University of Information Science and Technology, Nanjing 210044, China
[h] Institute of Advanced Study, Chengdu University, Chengdu 610106, China
[i] State Key Laboratory of Physical Chemistry of Solid Surfaces, College of Materials, Xiamen University, Xiamen, Fujian 361005, China
[j] ICREA, Pg. Lluís Companys 23, Barcelona 08010, Spain

ARTICLE INFO

Keywords:
Lithium-sulfur battery
Single-atom catalyst
Lithium polysulfide
Lithium plating
Electrocatalysis

ABSTRACT

The lithium-sulfur battery (LSB) has garnered considerable attention as prospective energy storage solution due to its outstanding theoretical energy density. However, the actual performance of LSBs falls short of meeting expectations, despite utilizing porous and highly conductive sulfur hosts to enhance their electrical conductivity and accommodate volume fluctuations. The primary factor contributing to the restricted performance is ascribed to the sluggish transformation of lithium polysulfides (LiPS) into sulfur and lithium sulfides. Single-atom catalysts (SACs) with outstanding activities and minimized weight offer an effective strategy to overcome this limitation. This work provides a comprehensive overview of the latest advancements in the field of SACS for LSBs, encompassing various aspects such as catalyst synthesis methods, battery performance evaluation, and mechanistic elucidation. The incorporation of SACs in the cathodes and separators facilitates the absorption of LiPS and enhances their conversion kinetics, thereby mitigating the adverse shuttle effect. In addition, SACs have a significant function at the anode by aiding the lithium stripping/plating process and concurrently preventing the development and enlargement of lithium dendrites. Overall, the design, engineering, and incorporation of SACs in LSBs and the understanding of their role are topics that deserve additional attention as a highly suitable strategy to boost LSB performance.

1. Introduction

The development of energy storage technologies, a vital link for a totally green and sustainable energy supply, is lagging behind the fast transformation of the energy sector. Early in the 1990s, lithium-ion batteries (LIBs) were commercialized and are presently employed in a wide array of uses, spanning from various portable gadgets to electric vehicles [1–3]. However, in the face of the relatively high cost, safety concerns, and moderate energy density of LIBs, the development of new generations of secondary batteries is required [4–6]. Among the several candidate architectures and chemistries, lithium-sulfur batteries (LSBs) relying on cathodes based on abundant and low-cost sulfur and carbon and characterized by high theoretical specific capacity (2600 Wh/kg) have become one of the most appealing options [7–9]. In contrast to the

* Corresponding authors.
** Corresponding author at: Catalonia Institute for Energy Research - IREC, Sant Adrià de Besòs, Barcelona 08930, Spain.
E-mail addresses: ecjsw@henu.edu.cn (J. Wei), yizhou.zhang@nuist.edu.cn (Y. Zhang), zhangqiaobao@xmu.edu.cn (Q. Zhang), acabot@irec.cat (A. Cabot).
[1] These authors contributed equally to this work.

https://doi.org/10.1016/j.ensm.2024.103240
Received 24 October 2023; Received in revised form 7 January 2024; Accepted 31 January 2024
Available online 1 February 2024

basic intercalation reaction of LIBs, LSBs are based on an electrochemical reaction between elemental sulfur and lithium to produce lithium sulfide (Li_2S) involving a multielectron transfer process [10]. During the discharge process, the lithium ions (Li^+) generated by the oxidation of metallic lithium on the negative electrode move to the positive electrode to react with sulfur. The reaction of Li^+ with sulfur (S_8) initially produces lithium polysulfide (LiPS) intermediates, which are subsequently converted into Li_2S. Through the reverse reaction, the battery is discharged (Fig. 1a): [11–13].

$$Li_2S \leftrightarrow Li_2S_2 \leftrightarrow LiPS \leftrightarrow S_8$$

Despite its high potential capacities, the energy density of real LSBs has been limited to 160–350 Wh/Kg, and the cycle life is far from satisfactory. The main reasons behind these limitations are the following: (1) The low electrical conductivity of sulfur (5×10^{-30} S/cm) and Li_2S (1×10^{-13} S/cm) hampers the electron transport and transfer during the electrochemical reaction, resulting in a low material utilization and slow reaction kinetics; [14,15] (2) The large volume change (80 %) between S and Li_2S can change the cathode architecture, electrically disconnecting part of the active material upon cycling; [16] (3) LiPS are highly soluble in the used electrolytes, thus part of the sulfur migrates back and forth between the positive and negative electrodes blocking the separator, corroding the metal lithium and decreasing the available active cathode material (Fig. 1b) [17–20].

To overcome these limitations, porous carbon nanomaterials are typically added to the cathode to increase electrical conductivity, promoting a faster electron transfer, and providing a buffer space for volume changes [21–25]. Nonetheless, carbon materials exhibit limited capability in adsorbing LiPS and catalyzing the Li-S reaction, leading to challenges in expediting the reaction and limiting the LiPS shuttle effect.

Furthermore, to fulfill the demands of practical implementations, it is necessary to enhance the areal sulfur loading and cathode sulfur content of existing laboratory LSBs to >5 mg/cm^2 and >70 % (mass fraction), respectively. Such relatively high sulfur content further limits the electrochemical performance of current LSBs and calls for the incorporation of highly effective catalytic additives able to accelerate the Li-S redox reactions to take full advantage of the active material while adding minimal additional weight and cost [26]

Transition metal-based catalysts have been thoroughly investigated as cathode additives to boost sulfur utilization and speed up the $Li_2S \leftrightarrow S_8$ conversion [27–31]. As an example, we demonstrated the use of flexible carbon nanofiber incorporating abundant MnS catalytic sites can accelerate the Li-S reaction kinetics and increase the LSB performance [32]. However, a careful investigation of the catalysts demonstrates that most of the introduced metal sulfide is inactive in this reaction, thus adding unnecessary weight. Generally, the processes of LiPS adsorption and conversion occur at the catalyst's surface. Thus, even relatively small catalyst particles are characterized by moderate metal utilization rates, unnecessarily increasing the weight and cost of the battery and thus reducing its specific energy density.

Since Zhang et al [33] first reported the preparation of a platinum single-atom catalyst (SAC) in 2011, numerous works have demonstrated a variety of strategies for producing various SACs supported on various substrates, distinguished by their high catalytic activity. Shrinking particles to the sub-nanometer scale allows for maximizing the amount of exposed catalytic sites. Moreover, the low coordination environment of SACs is associated with large surface energies and frequently lower reaction barriers [34]. Besides, the unique gap between the highest-energy occupied and lowest-energy unoccupied molecular orbital of SACS results in a charge redistribution with the support and a

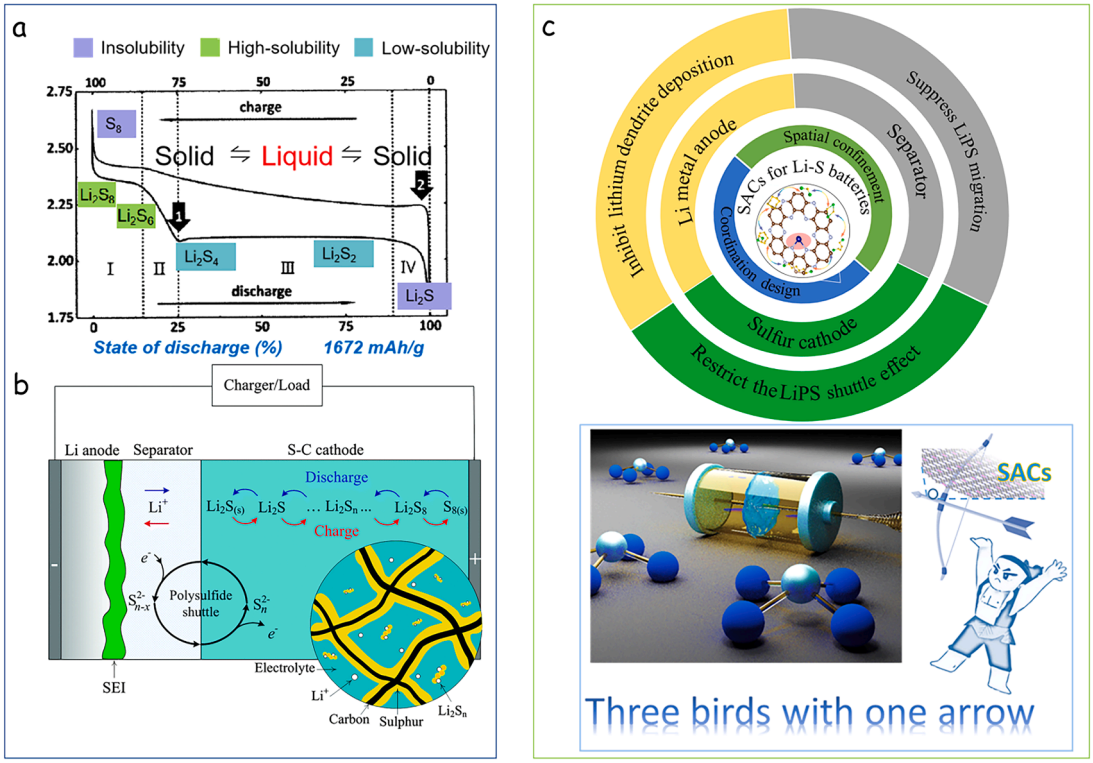

Fig. 1. (a) A typical discharge/charge profile of LSBs with different LiPS at different voltage regions. The black vertical arrows (1 and 2) point at the capacities of the first and second discharge plateaus. While discharging, sulfur initially transforms into lithiated sulfur, creating a sequence of intermediate lithium polysulfide compounds ($S_8 \rightarrow Li_2S_8 \rightarrow Li_2S_6 \rightarrow Li_2S_4$). These compounds easily dissolve in ether-based electrolytes. This stage corresponds to the upper voltage plateau, accounting for 25 % of sulfur's theoretical capacity. At the lower voltage plateau, responsible for the remaining 75 % of sulfur's theoretical capacity, further lithiation leads to the transformation of long-chain polysulfides into solid lithium sulfides that re-deposit on the electrode ($Li_2S_4 \rightarrow Li_2S_2 \rightarrow Li_2S$). (b) Schematic of the LiPS dissolution and migration within LSBs. Reproduced with permission [17] Copyright 2015, The Royal Society of Chemistry. (c) Schematic of the uses of SACs to address the key challenges on LSBs.

high polarity suitable to adsorb polar molecules such as LiPS [35]

Compared with heteroatom (O, N, etc.)-doped carbon materials, metal-based SACs have both adsorption and catalytic effects, promoting redox reactions by forming strong chemical bonds between polysulfides/sulfides and individual metal atoms, as well as forming local coordination structures that are prone to reactant decomposition. Compared with metal derivatives with the same adsorption capacity and catalytic effect, sub-nanoscale SACs expose a much larger number of catalytic sites with a minimum effect on the overall weight and thus the energy density of the battery.

Herein, we provide an overview of the advancements in the study of single-atom materials, specifically focusing on SACs, within the context of LSBs. The discussion encompasses topics such as the synthesis of these materials, techniques for characterization, potential application pathways, and the underlying catalytic mechanisms (Fig. 1c). Besides, the difficulties encountered by single-atom materials in battery applications are examined, along with prospective strategies and avenues for future research endeavors.

2. Preparation and identification of SACs

2.1. Synthesis of SACs

SACs merge the beneficial traits of both heterogeneous and homogeneous catalysts, yielding superior performance compared to conventional heterogeneous counterparts. Fig. 2 displays a brief timeline of the LSBs and SACs development. SACs play an increasingly important role in the field of catalysis due to their excellent catalytic performance. Consequently, integrating SACs could prove indispensable in crafting LSBs capable of fulfilling upcoming commercial requisites. However, the formation of metal clusters is energetically favored compared to the isolated formation of single atoms (SAs). Isolated SAs exhibit substantial free energies, making them prone to aggregation, both during synthesis and usage in electrochemical procedures [36]. Thus, novel synthetic methodologies must be embraced to accomplish the dispersion and separation of atomic-level precursors. Furthermore, it is equally crucial to limit the diffusion and aggregation tendencies of resultant SAs during SACs' operation. To address this issue, diverse approaches centered around spatial confinement and coordination design have been developed to proficiently disperse and stabilize SAs onto carbon substrates throughout the preparation phase.

2.1.1. Spatial confinement strategy

The spatial confinement strategy entails the encapsulation of SAs within molecular/nano/micro cages to impede their mobility. This strategy generally involves first a proper dispersion of the atomic precursor within large surface area materials and subsequently a generally thermal or chemical process to activate the SA preventing agglomeration through anchoring it to the support. Proper support can synergistically boost the overall catalyst performance, thus its selection is fundamental. In this direction, metal-organic frameworks (MOFs) are commonly utilized as substrates for the stabilization of SACs [37–39]. MOFs possess a precisely defined porous architecture that facilitates the spatial isolation and encapsulation of mononuclear metal precursors. Besides, following the process of pyrolysis, a significant number of coordination sites are produced, which can effectively anchor SACs. As an example, Yang et al [40] successfully synthesized N-doped hollow carbon spheres (HPC) with up to 11.3 % (mass fraction) loading of Zn SAs through the pyrolysis of ZIF-8. As depicted in Fig. 3a, the authors first assembled ZIF-8 nanoparticles on the surface of polystyrene (PS) nanospheres to create PS@ZIF-8 core-shell composites. Subsequently, the composite was immersed in N,N-dimethylformamide to remove the PS core, resulting in hollow ZIF-8 structures. Finally, during high-temperature sintering, the ligand 2-methylimidazole was transformed into hollow carbon spheres rich in N sites, and the metal Zn atoms were uniformly dispersed on the hollow carbon spheres through Zn-N_4 coordination structures.

Zn-based bimetallic MOFs are commonly used as precursors for SACs due to the easy selective removal of Zn during pyrolysis. These MOFs are generally formed through the coordination of 2-methylimidazole linkers with metal ions that have similar ionic radii as Zn^{2+} [41,42]. Zn atoms and 2-methylimidazole linkers effectively induce spatial separation among the desired metal atoms, thereby resulting in an increased interatomic distance. At elevated temperatures, Zn evaporates, resulting

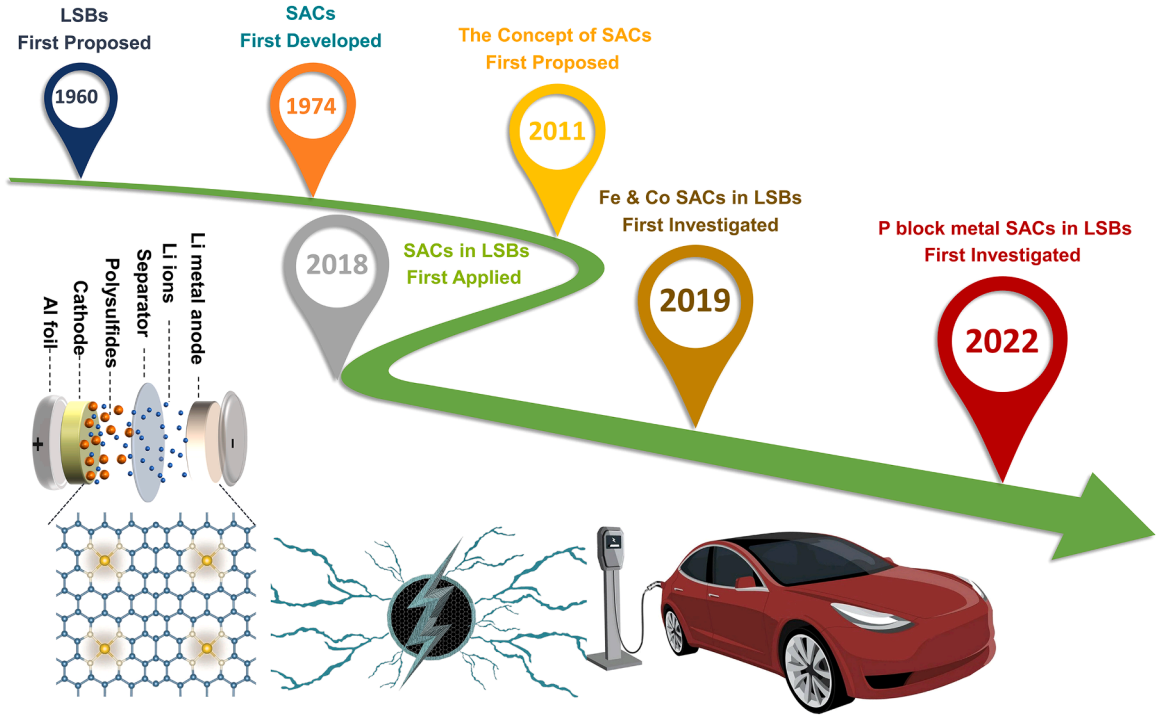

Fig. 2. Recent progress in the development of SACs for LSBs.

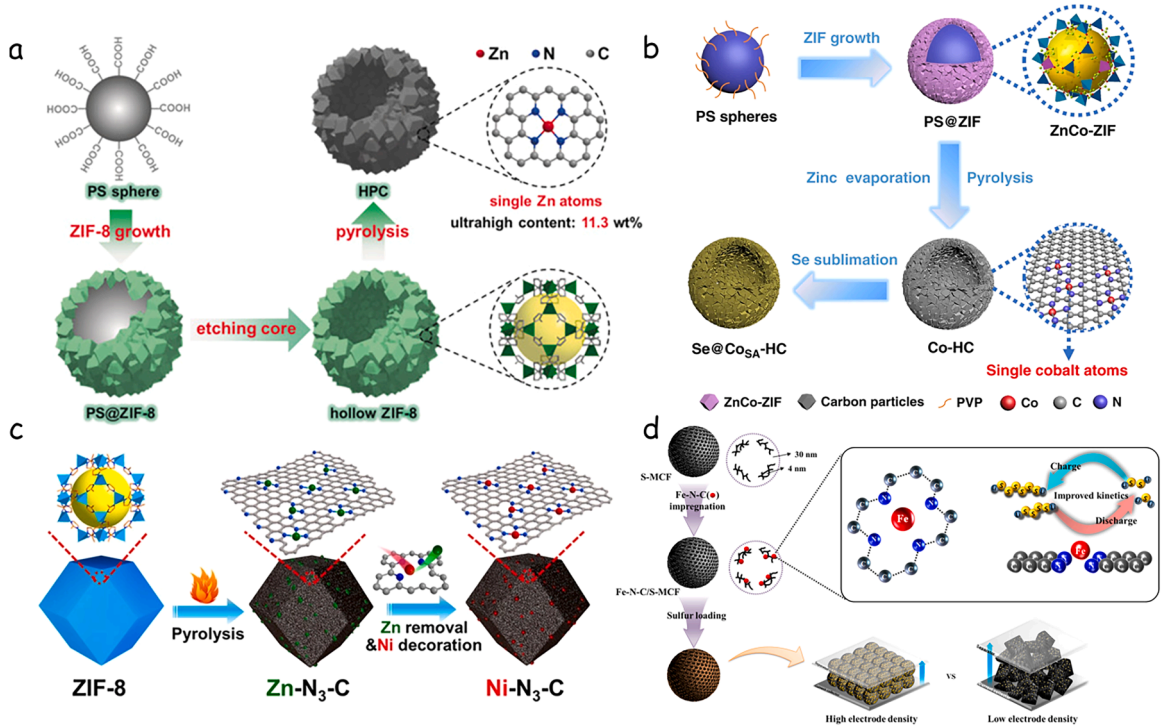

Fig. 3. (a) Schematic illustration showing the synthesis of HPC. Reproduced with permission [40]. Copyright 2028, Wiley-VCH. (b) Schematic illustration of the procedures for synthesizing cobalt SAs/nitrogen-doped hollow porous carbon (CoSA-HC). Reproduced with permission [42] Copyright 2020, Nature Publishing Group. (c) Fabrication of low-coordination single-atom Ni electrocatalysts (Ni-N_3-C). Reproduced with permission [45]. Copyright 2021, Wiley-VCH. (d) Synthesis of SA-Fe@spherical mesoporous carbon using the spatial confinement strategy. Reproduced with permission [47] Copyright 2018, American Chemical Society.

in a dispersion of the targeted metal atoms onto the generated carbon framework. Besides, the carbon support undergoes significant nitrogen doping, resulting in an effective immobilization of the metal atoms that prevents their diffusion and aggregation.

One of the most widely studied bimetallic MOFs based on zinc is the Zn/Co-ZIF [43,44]. As an example, Tian et al. synthesized advanced electrocatalysts comprising solitary cobalt (Co) atoms anchored on nitrogen-doped hollow porous carbon (CoSA-HC) using high-temperature pyrolysis (depicted in Fig. 3b) [42]. This process involved generating Zn/Co-ZIF clusters atop PS spheres, where the metal atoms were coordinated with polyvinylpyrrolidone. Consequently, this procedure produced a consistent ZIF coating on the PS sphere's surface.

Subsequently, the hybrid structure was carbonized during pyrolysis under N_2 at 700 °C. Afterward, HF was employed to etch the PS template, producing hollow structures. During high-temperature sintering, the evaporation of Zn facilitated the uniform anchoring of N-coordinated Co atoms onto the carbon skeleton in the form of Co-N_4 moieties.

Additional SACs have been produced by incorporating various transition metals, including Mn, Ni, and Fe, into Zn-based bimetallic MOFs. As an example, catalysts featuring single nickel atoms with low coordination numbers on N-doped carbon supports were synthesized via the process of post-synthesis metal substitution (Fig. 3c) [45]. Initially, during pyrolysis, Zn nanoparticles formed and easily evaporated, resulting in N-doped carbon with abundant Zn-N_3-C sites. Subsequently, the remaining Zn atoms were easily etched using HCl due to their fragile coordination with N. The generated voids were filled with Ni atoms, yielding Ni-N_3-C structures where single Ni atoms are coordinated by three N atoms which enable its high dispersion on the N-doped carbon.

Apart from MOF structures, SAs are frequently dispersed through the utilization of self-assembled micro-cages. For example, Shao et al. synthesized mesoporous hollow carbon spheres (MHCS), which were subsequently subjected to heating under Ar and NH_3 streams to yield N-doped MHCS. In the subsequent steps, a solution of iron phthalocyanine dissolved in tetrahydrofuran was introduced to generate a precursor. This precursor underwent centrifugation and drying, followed by pyrolysis to yield Fe-N/MHCS [46]. Remarkably, the resultant Fe-N/MHCS retained the structural integrity of the spherical and mesoporous carbon shells. The presence of iron in the form of SAs was further validated by the absence of Fe nanoparticles, as confirmed by transmission electron microscopy (TEM) images of Fe-N/MHCS.

SACs can also be confined within micro/mesoporous carbon structures through the impregnation of metal salts or molecular precursors. Lee et al. employed a bottom-up methodology to produce mesoporous carbon particles including Fe-N-C moieties, intended for use as sulfur hosts in LSBs (depicted in Fig. 3d) [47]. The process began with the incorporation of metal complexes, specifically Fe(II) phthalocyanine, into the support. This was followed by thermal treatment in Ar/NH_3 to yield uniform Fe-N-C catalytic sites within the carbon structure.

2.1.2. *Coordination design strategy*

Another effective strategy to block the diffusion of SAs and prevent their aggregation is the design of coordinating architectures that include SA anchors. This strategy requires the initial design and engineering of supports containing large and uniform dispersions of coordination sites. The SA precursor and the coordination site should be properly selected to achieve and preserve a strong bonding during the subsequent production steps in the required synthesis conditions. As in the spatial confinement strategy, a proper selection of the support, and specifically of the SA anchors is fundamental to optimizing the SAC performance.

In this direction, non-metal atoms with lone pair electrons, *e.g.* N, O, P, and S have a strong ability to coordinate with metal atoms. Among these, nitrogen atoms stand out due to their high electronegativity and size similarity to carbon atoms, which makes them more easily integrated into the carbon lattice, leading to the formation of stable N-doped carbon materials. This integration of nitrogen disrupts the electrical balance in carbon-based materials, altering their electronic configuration and distribution. As a result, new active sites are formed, enhancing the number of available active sites and boosting the kinetics of

polysulfide conversion reactions. Specifically, N-doped carbons with pyridinic, pyrrolic, and graphitic nitrogen contain abundant metal anchoring sites [48,49]. This carbon-coordinated N is generated during pyrolysis under an NH_3 atmosphere. Alternatively, it can be produced through the pyrolysis of melamine (MA), [50] polymers, [51] or g-C_3N_4 under an Ar atmosphere [52,53]. As an example, Zhang et al. obtained N-doped graphene (NG) from dicyandiamide and glucose, and introduced single Ni atoms using a precursor salt, $NiCl_2{\cdot}6H_2O$. Subsequently, the precursor was annealed under an Ar atmosphere to obtain SA-Ni-NG, where Ni atoms were uniformly confined within the NG substrate through Ni-N_4 coordination [52]. Lu et al. reported a simple method to produce SAFe@g-C_3N_4. First, they obtained the precursor by mixing iron (II) acetate and g-C_3N_4 in an ethanol solution. The subsequent annealing of the precursor (Fig. 4a) resulted in SAFe@g-C_3N_4, displaying a layered structure with abundant single iron atoms uniformly dispersed. Besides, Wu and colleagues prepared Co@C_3N_4 via a two-step process involving the mixing of melamine and cyanuric acid with a Co^{2+} precursor in a DMSO and the posterior annealing of the formed 2D architecture (MA/CA) in an Ar atmosphere (Fig. 4b) [54,55]. During the thermal process, MA/CA transformed into C_3N_4 with a tri-s-triazine structure, and Co SAs remained attached to the support. SACs including Fe-N-C sites were produced in a multi-step process from the reaction of 1,8-diaminonaphthalene and 2,6-diacetylpyridine, the impregnation of the obtained bis(imino)pyridine with a Fe^{3+} salt ($FeCl_3{\cdot}6H_2O$), and the subsequent annealing and acid leaching of the final product (Fig. 4c) [56]

Beyond, N-doped carbon materials, graphene oxide (GO), characterized by O-containing functional groups, presents numerous sites for the dispersion of SAs. For instance, Wan et al. synthesized SA-Co@NG, incorporating Co-N-C sites, which were then assessed as sulfur hosts in LSBs [57]. This was achieved by introducing Co SAs into NG via the addition of $CoCl_2{\cdot}6H_2O$ to an aqueous GO suspension, followed by freeze-drying the mixture and annealing it under an Ar/NH_3 atmosphere. Dou et al. developed a top-down technique to produce SA-Co@hollow carbon sphere (HC)@S for application as cathode materials in Na-S batteries (as depicted in Fig. 4d) [58]. In this method, a $CoCl_2$ solution was combined with hollow carbon spheres, and the resultant mixture underwent thermal treatment to reduce the Co salt into Co nanoparticles, leading to a uniform decoration of the carbon shells (Co@HC). Subsequent loading of molten sulfur into Co@HC, followed by a thermal process, enabled sulfur molecules to interact strongly with Co nanoparticles. At temperatures around 300 °C, these sulfur molecules initiated diffusion, facilitating atomic Co migration onto the carbon shells and consequently achieving a uniform dispersion of Co SAs.

Several strategies involving spatial confinement and coordination design have been employed to disperse SAs across different host materials. Among these strategies, the spatial confinement of SAs offers

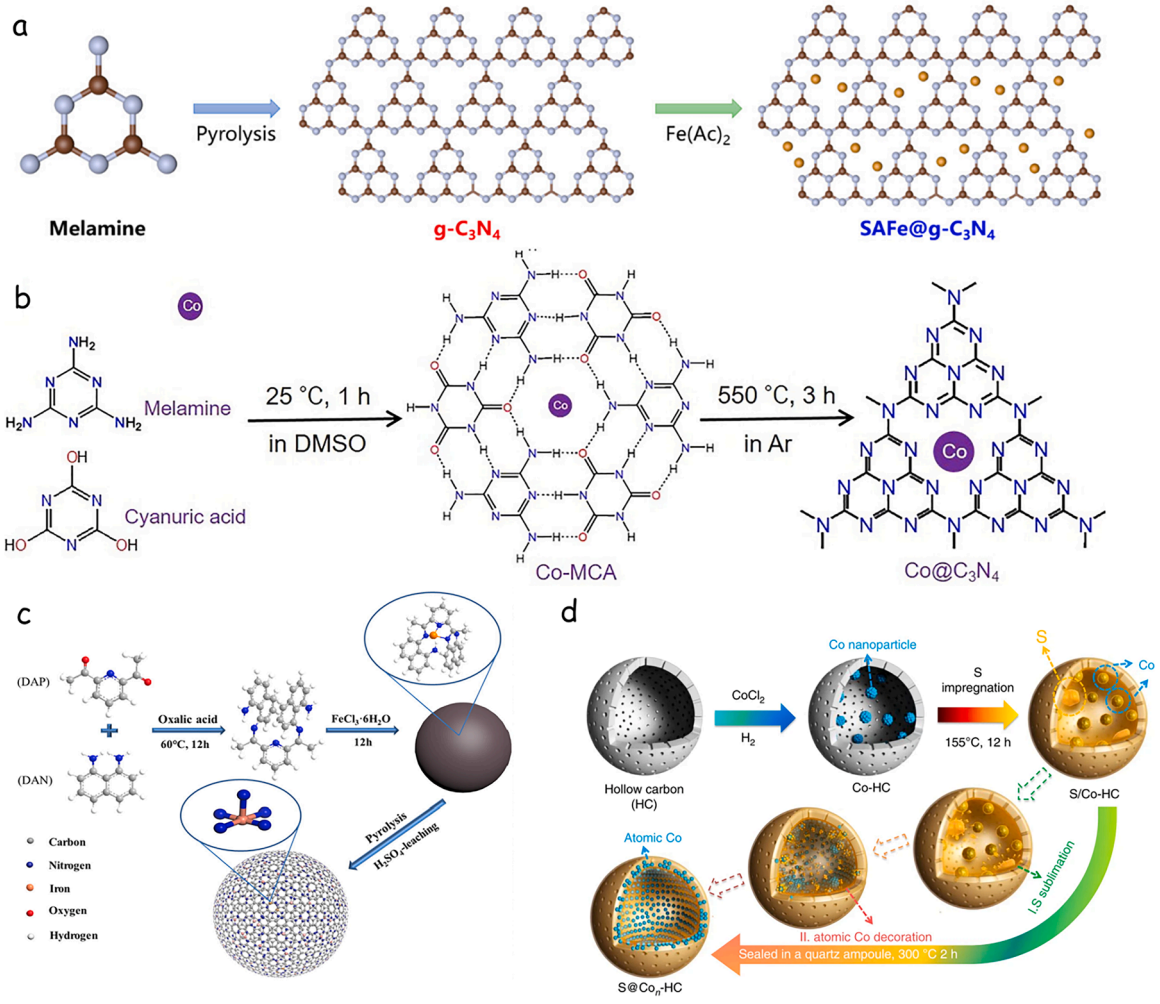

Fig. 4. (a) Process of synthesizing SAs Fe dispersed on g-C_3N_4 (SAFe@g-C_3N_4) materials. Reproduced with permission [54] Copyright 2020, American Chemical Society. (b) Schematic synthetic procedure for Co@C_3N_4. Reproduced with permission [55] Copyright 2019, Elsevier. (c) Schematic illustration for the synthesis of Fe-N-C catalysts. Reproduced with permission [56] Copyright 2018, Elsevier. (d) Fabrication of SA-Co@HC@S employing the coordination design strategy. Used with permission [58] Copyright 2018, Nature.

advantages such as more uniform distribution. However, this approach often necessitates a high-temperature pyrolysis step and meticulous reaction conditions to eliminate ligands from the precursor and form micro-cages capable of encapsulating SAs. This complexity impedes the feasibility of cost-effective large-scale production. In contrast, the coordination design strategy offers control over the coordination structure, the quantity of anchored metal atoms, and the interactions between these atoms and ligands. This approach enables the creation of diverse SACs with precise structures and functions [59]. When these two strategies are amalgamated, the result is SACs featuring a heightened dispersion of SAs, consequently leading to increased loading. Moreover, uniform dispersion and loading of SAs contribute to the augmentation of chemical kinetics and the efficient utilization of active sites within LSBs. Apart from the aforementioned strategies, alternative techniques including atomic layer deposition (ALD), [60] ball milling, [61] and microwave-assisted synthesis, [62] have also been reported for the fabrication of SAC@carbon materials.

2.2. Characterization of SACs

The conventional methods for *in situ* and *ex situ* examining nanoscale catalysts are often inadequate in terms of spatial resolution and signal intensity when it comes to characterizing SACs. *Ex situ* structural characterization allows us to confirm the presence of SAs on a substrate, as well as determine their chemical state and spatial distribution. In parallel, *in situ* characterization offers valuable insights into the dynamic alterations of both reactants and SACs throughout the electrochemical process. This type of analysis provides essential information for comprehending the catalytic mechanism.

2.2.1. Ex situ characterization of SACs

Advanced techniques with ultrahigh resolution have been innovated to examine the electronic structure and localized surroundings of metal SAs. Among these, aberration-corrected high-angle annular dark-field scanning transmission electron microscopy (AC-HAADF-STEM) and energy-dispersive X-ray (EDX) spectroscopy are frequently utilized. These techniques prove instrumental in assessing the existence and spatial distribution of monatomic materials on their respective supports. AC-HAADF-STEM operates by detecting incoherently scattered electrons, generated through the interaction between the incident electron beam and the SA via Rutherford scattering. These scattered electrons are collected by a detector to form an image, where SAs appear as bright spots (Fig. 5a). As an example, in a study by Li et al [63], various metals on N-doped carbon nanosheets (NCNS) support were obtained through an ALD process. Fig. 5b depicts AC-HAADF-STEM dark-field images of the samples, revealing the dense features of the isolated atoms. Also, low-magnification EDX elemental mapping of NC-based SACs proved the absence of aggregates and the uniform metal distribution. Moreover, electron energy loss spectroscopy (EELS) detected signals of Co L_2 and L_3 on Co_1Pt_1/NCNS, further confirming the existence of isolated Co atoms.

X-ray photoelectron spectroscopy (XPS), mössbauer spectroscopy, and synchrotron-radiated X-ray absorption spectroscopy (XAS) are valuable techniques for investigating the coordination structure and electronic state of SAs. XPS enables qualitative analysis of the elemental composition and chemical valence state of the sample surface. By using X-ray photons with specific energy, electrons from the atomic orbitals of the sample can be excited, allowing the determination of their binding energy. Thus, the chemical environment of surface elements can be inferred from the position of XPS peaks. The chemical valence state and electronic structure of SAs can be further assessed using XAS. XAS involves exciting the inner shell electrons of SAs with X-ray photons, leading to changes in energy (absorption edge) and the emergence of oscillatory structures. The XAS spectrum comprises absorption edges and oscillatory structures, which can be categorized into X-ray absorption near-edge structures (XANES) in the 40–1500 eV range of the absorption edge and X-ray absorption fine structures (EXAFS) located within ± 50 eV of the absorption edge.

Although HAADF-STEM and synchrotron radiation EXAFS show that SAs are distributed in a single atomic state, its coordination environment and whether all SAs are indeed atomically dispersed are still unclear. In a study conducted by Chen et al., [35] room temperature Mössbauer spectroscopy was performed to reveal the coordination environment of Sn SACs, which demonstrated that the coordination of atomically dispersed Sn^{4+} sites with four oxygen atoms (Fig. 5c,d). This study proved that Mössbauer spectroscopy is reliable and indispensable for accurately characterizing the purity of SACs.

In Fig. 5e–g, Li et al [63] synthesized a range of metal SAs anchored onto porous N-doped carbon nanosheet supports (NCNS), demonstrating their efficacy as efficient catalysts for the oxygen reduction reaction (ORR). XANES spectra captured at the K-edge compared the catalyst to a reference sample. The k^3-weighted Fourier transform EXAFS spectrum of Co_1Pt_1/NCNS, Fe_1Pt_1/NCNS, and Ni_1Pt_1/NCNS, a prominent peak emerges at 1.57 Å, 1.52 Å, and 1.59 Å, respectively, signifying the coordination of dispersed Co, Fe and Ni atoms on the carbon support. To delve deeper into the local coordination environment, wavelet transform analysis of the k^3-weight EXAFS signal was conducted (Fig. 5h–j). The results further proved atomically dispersed Co, Fe and Ni SAs, unlike their oxide and foil. Consequently, it can be concluded that Co, Fe, and Ni atoms within Co_1Pt_1/NCNS, Fe_1Pt_1/NCNS, and Ni_1Pt_1/NCNS exhibit coordination with N atoms.

For precise assessment of the SAs content on a substrate, XPS and inductively coupled plasma-optical emission spectroscopy (ICP-OES) are commonly employed. ICP-OES operates by exciting ions and atoms, resulting in emitted light at specific wavelengths, facilitating the quantification of element concentration through measurement of light intensity proportionate to the concentration of the element [64,65]. This technique allows simultaneous analysis of multiple elements and is known for its high sensitivity and stability, making it suitable for accurate determination of metal loading in SACs. In contrast, thermogravimetric analysis (TGA), which is typically used to determine sulfur content in LSB cathodes, has relatively lower accuracy and sensitivity, and is not frequently employed for analyzing SA loading in SACs.

2.2.2. In situ characterization of SACs

Advanced *in situ* characterization techniques such as *in situ* X-ray diffraction (XRD), *in situ* XAS, and *in situ* Raman spectroscopy are emerging as powerful tools for acquiring real-time insights into reaction kinetics during electrochemical processes. These techniques facilitate the investigation of catalytic effects and mechanisms of SACs in sulfur electrodes by tracking the structural changes of sulfur species and SACs throughout electrochemical reactions.

The development of various cell designs for *in situ* XRD analysis is of particular interest as it allows for the adaptation of battery chemistry and form factors to facilitate *in situ* measurements. Several designs have been employed, as shown in Fig. 6a [66]. For instance, Fig. 6b presents *in situ* XRD patterns of the S@HP-SAFe and S@HP-SANi cathodes, where the cells were first discharged at a rate of 0.1 C, measured at various voltages. During the discharge step, the XRD patterns of the S@HP-SAFe cathode display the transition from S_8 to Li_2S. In contrast, the S@HP-SANi cathode shows less intense Li_2S XRD peaks after complete discharging, thus a moderate polysulfide conversion ability. *In situ* XANES spectroscopy is instrumental in discerning the oxidation state of SACs during electrochemical processes, offering insights into the interaction between SACs and sulfur species. *In* XAS has substantially enriched our comprehension of the multi-step redox electrochemical reactions in LSBs. For instance, Cuisinier et al. employed *in situ* XAS to delve into LSBs, illuminating sulfur speciation and its impact on the dissolution and deposition of sulfur and Li_2S [67]. This study employed a modified coin cell (Fig. 6c) equipped with an aluminized Kapton window to enable X-ray penetration [66].

In the sulfur K-edge spectra shown in Fig. 6d, *in situ* XAS spectra show the precipitation of Li_2S is delayed during discharge due to the

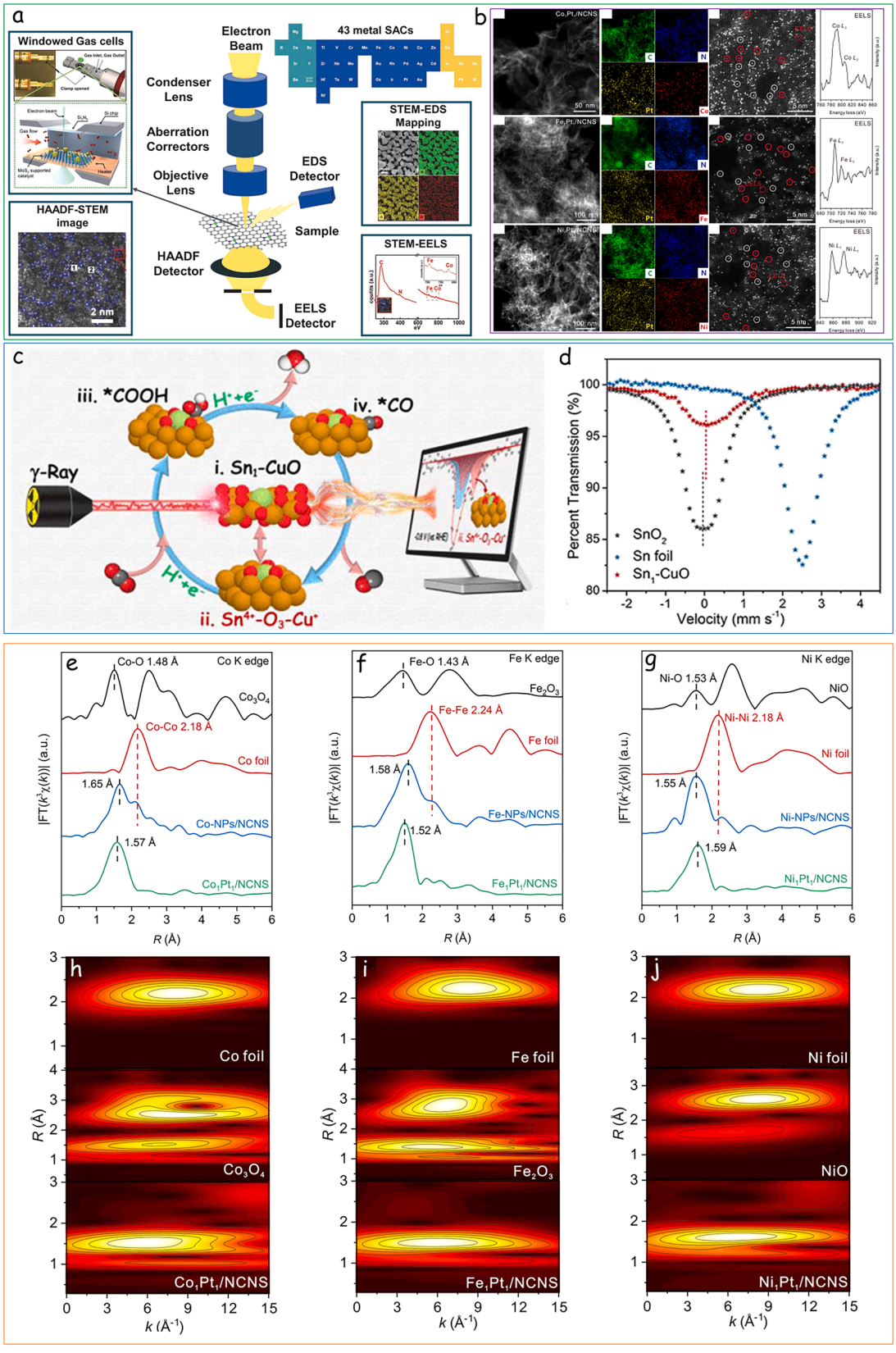

Fig. 5. (a) Schematic illustration of a TEM equipped with aberration corrector(STEM techniques frequently used for SACs characterization are illustrated, including HAADF-STEM, STEM-EELS and STEM-EDX). Reproduced with permission [34] Copyright 2022, Springer. (b) HAADF-STEM images, corresponding EDX mapping and EELS spectra of different metals atoms on N-doped carbon nanosheets. Reproduced with permission [63] Copyright 2021, Springer Nature. (c,d) Room-temperature ^{119}Sn Mössbauer spectra of Sn foil, SnO_2, and 5.25 % S-CuO (Sn_1-CuO). Reproduced with permission [35] Copyright 2023, American Chemical Society. (e-g) The k^3-weighted Fourier transform of EXAFS spectra at Co/Fe/Ni K-edge of different SACs. (h-j) Wavelet-transformed spectra of various SACs and the reference materials. Reproduced with permission [63] Copyright 2021, Springer Nature.

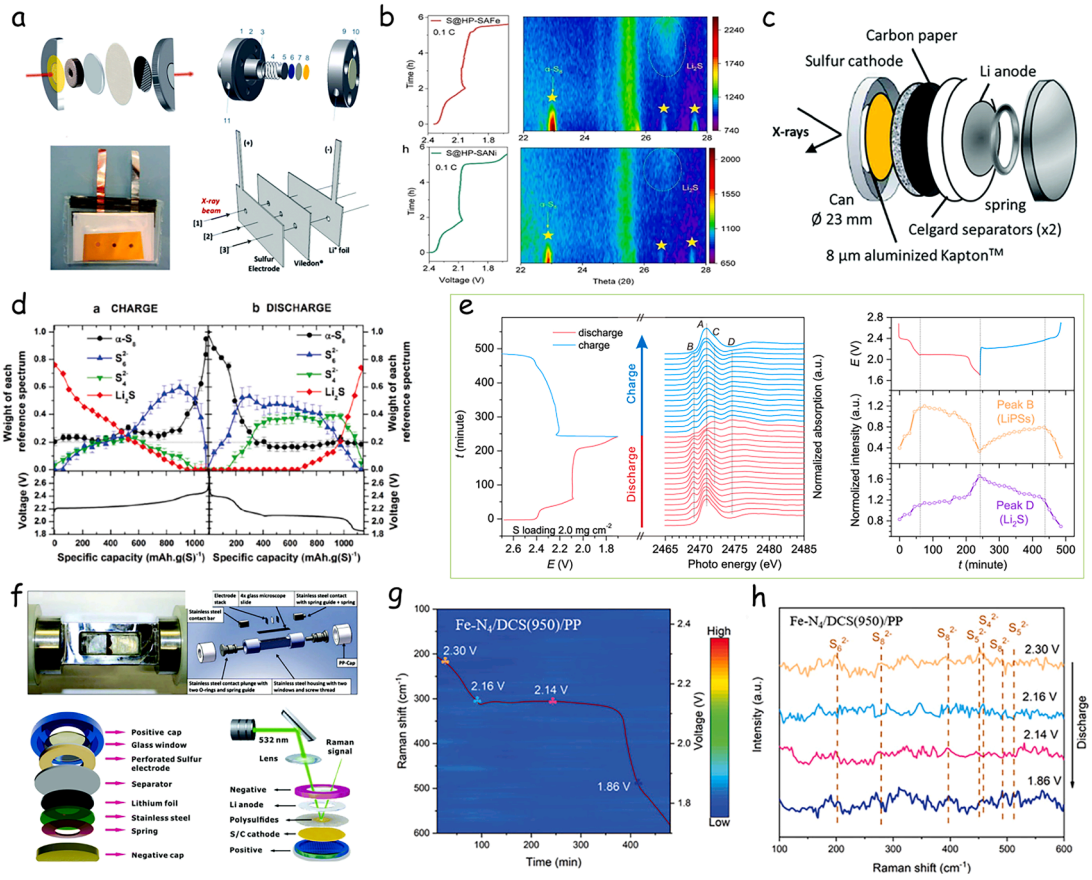

Fig. 6. Schematic configurations of the (a) *in situ* XRD, (c) *in situ* XAS, and (f) *in situ* Raman spectroscopy setups are depicted. This reproduction is authorized copyrighted by the Royal Society of Chemistry [66] (b) *In situ* XRD patterns and galvanostatic charge/discharge curves of S@HP-SAFe and S@HP-SANi cathodes. Reproduced with permission [39] Copyright 2023, Wiley-VCH. (d) *In situ* XANES spectra of the sulfur K-edge XAS spectra upon electrochemical cycling based on linear combination analysis. Reproduce with permission [68]. Copyright 2019, Wiley-VCH. (e) *In situ* XANES spectra of the S K-edge of a SA-Co@NG cathode (left). Evolution of the intensities of peak B and peak D during electrochemical cycling (right). Reproduced with permission [57]. Copyright 2019, American Chemical Society. *In situ* time-resolved Raman spectra at 0.1 C during the discharge of the cells with (g) Fe-N_4/DCS (950) separators. Selected Raman signals of the cells at different voltage states with (h) Fe-N_4/DCS (950) separators. Reproduce with permission [69]. Copyright 2023, Wiley-VCH.

supersaturation of S^{2-}, while the surface oxidization of Li_2S proceeds straightforwardly with the formation intermediate LiPS, *i.e.*, Li_2S_4 and Li_2S_6 [68]. Similarly, *in situ* XANES analyses were undertaken by Wan et al [57] to investigate the LiPS catalytic conversion on SA-Co@NG. The change in the concentration of intermediates was assessed by monitoring the change in intensity of specific peaks (Fig. 6e). A distinct increase in peak D during the initial discharge stages was associated with the formation of Li_2S, emphasizing the increased kinetics in the transformation from soluble LiPS to insoluble Li_2S facilitated by SA-Co. Raman spectroscopy is a powerful optical technique that can provide qualitative or semi-quantitative analysis of soluble LiPS during cycling [69,70]. Hagen et al [71] engineered an *in situ* electrochemical Raman setup for LSBs, employing a rectangular stainless steel chamber (Fig. 6f) [66]. Zhang et al [72] reported an LSB utilizing a separator modified with SA-Fe@NG, along with the corresponding Raman spectra recorded at different measurement points (A1-A9). Through the comparison of the different Raman spectra of a separator modified with SA-Fe@NG and a commercially available separator, the catalytic properties of SA-Fe@NG were found to facilitate improved kinetics of LiPS conversion and enable complete sulfur conversion. Moreover, Fig. 6g,h reveals a faint signal from polysulfides detected from the separator loaded with Fe-N_4/DCS (950) throughout the whole discharge cycle. This suggests that Fe-N_4/DCS nanosheets are capable of catalyzing the swift conversion of polysulfides, preventing their migration.

Combining *ex situ* and *in situ* experimental techniques and theoretical calculations are crucial to confirm the presence of SACs, assessing their local coordination environment, and understanding their catalytic mechanisms. Besides, a comprehensive understanding of the atomic and molecular-level catalytic mechanisms of SACs is essential to designing and engineering optimized SACs with maximized performance.

3. Applications in LSBs

Unlike metal nanoparticles and clusters, SACS utilize individual metal atoms as their active sites. In the context of redox reactions, nanoparticles or clusters are limited because only their surface metal atoms serve as active sites. Consequently, under identical metal-loading conditions, SACs offer a greater number of active sites for these reactions. SACs represent the pinnacle of metal dispersion and optimize atom usage. Furthermore, their development significantly cuts down on the need for costly precious metals, thus reducing production expenses. SACs are distinguished by their exceptional catalytic activity, surpassing that of conventional supported catalysts. SACs can play a role both at the cathode and anode sides of LSBs, while supported on their surface or within a SAC-modified separator. At the cathode side, their high reactivity enhances the binding of LiPSs, inhibiting their migration and boosting conversion kinetics. At the anode side, SACs with evenly distributed lithiophilic sites lower the interface energy between Li and its deposition matrix, reducing Li nucleation overpotential. Thus, a sufficiently high concentration of SACs, evenly spread at the nanometer level, can prevent dendrite formation. Conversely, a non-uniform micron-scale distribution of metal SAs on the Li anode surface could

create irregular lithiophilic sites, leading to uneven lithium nucleation and disordered Li dendrite growth.

3.1. SACs for lithium anodes

Lithium metal is an almost ideal candidate for LSB anodes due to its low electrochemical potential (-3.040 vs SHE) and substantial theoretical capacity. Nevertheless, the extensive adoption of lithium anodes is hampered by a series of challenges, which encompass reduced Coulombic efficiency during lithium deposition and stripping, the emergence of dendritic structures, notable volume shifts in lithium, and the development of unstable solid electrolyte interphases (SEI) [73,74]. To confront these obstacles, a practical approach involves integrating an appropriate host material with the ability to accommodate the notable volumetric fluctuations of lithium, effectively regulating the deposition and extraction of Li^+ ions throughout the cyclic process.

Numerous approaches have been suggested to ease the occurrence of dendritic formations on lithium metal anodes. Within this context, SACs showcase substantial promise across diverse avenues. Huang and colleagues demonstrated that SA Zn not only aids in the creation of a coherent and compact SEI but also promotes the uniformity of Li^+ flow, thereby enhancing the evenness of lithium deposition (Fig. 7a) [75]. Density functional theory (DFT) analyses provided insights into the phenomenon of Li deposition, indicating that the presence of SA Zn sites can significantly reduce the nucleation barrier of lithium and promote ultra-uniform nucleation.

Accordingly, a layer of densely ultra-thin lithium is efficiently generated on the lithium nuclei, diffusing upwards and growing seamlessly. This outcome translates into the Zn SAC working electrode displaying improved deposition kinetics, resulting in a reduced nucleation overpotential of around 7.7 mV. Nucleation overpotential is closely linked to the energy barrier for Li deposition on heterogeneous

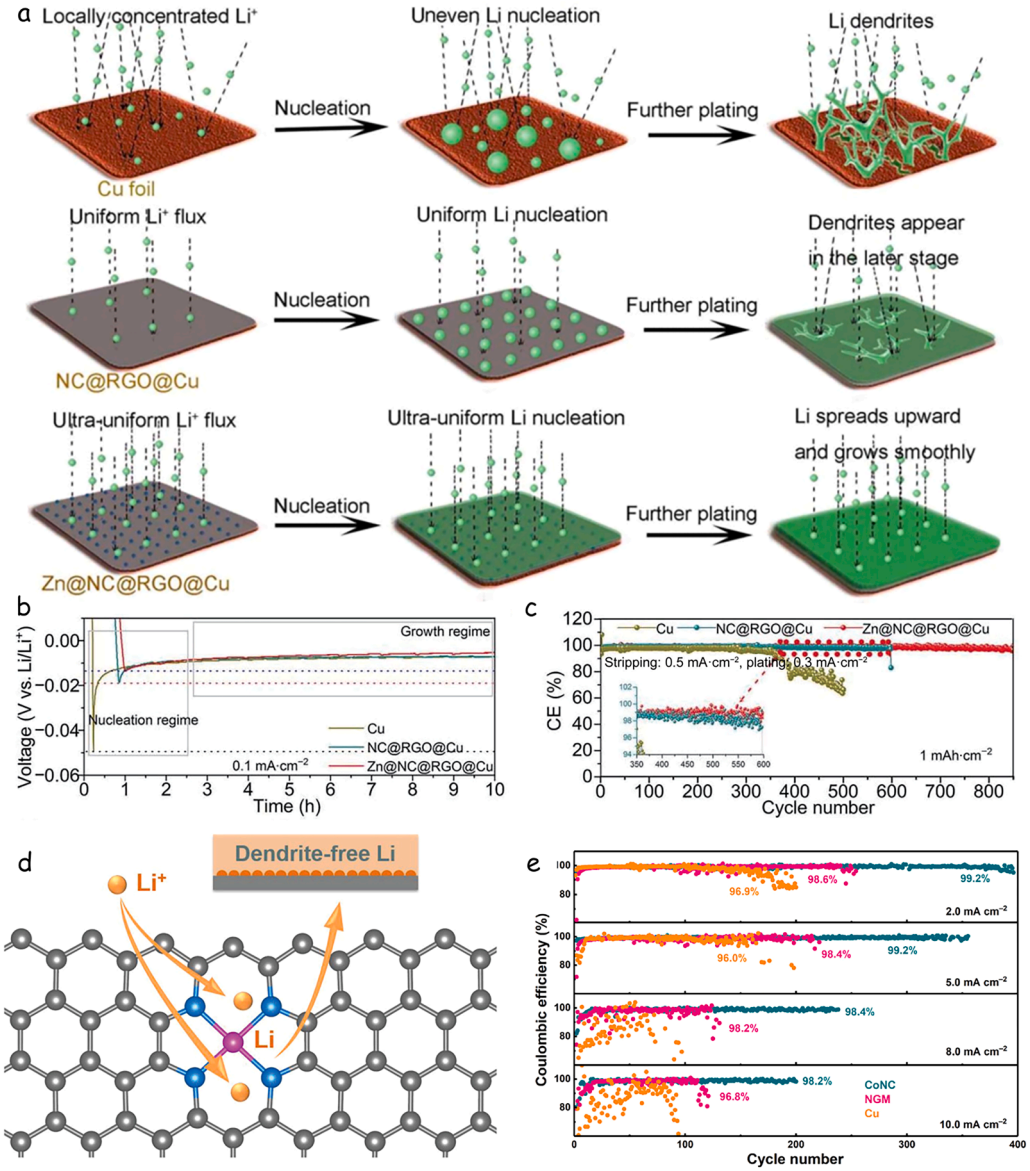

Fig. 7. (a) Schematic illustration of lithium deposition on Cu foil, NC@RGO@Cu, and Zn@NC@RGO@Cu electrodes is presented (Fig. 7a). Voltage-time profiles during lithium plating at a current density of 0.1 mA·cm^{-2} are shown (Fig. 7b). Coulombic efficiencies (CEs) and charge-discharge specific capacity curves during Li plating at 0.3 mA·cm^{-2} and stripping at 0.5 mA·cm^{-2} are displayed (Fig. 7c). This reproduction is authorized, [75] copyrighted by Tsinghua University Press. Schematic representation of CoNC and preferential Li nucleation sites is illustrated (Fig. 7d). Gray represents carbon, blue denotes nitrogen, and deep pink signifies cobalt. CE comparisons of CoNC, N-doped graphene matrix, and Cu electrodes at different current densities with a fixed capacity of 2.0 mAh cm^{-2} are presented (Fig. 7e). This reproduction is authorized, [76] copyrighted by Wiley-VCH.

substrates, revealing the substantial enhancement of lithium nucleophilic sites due to the integration of single atomic lithiophilic Zn-coordination sites. This enhancement promotes stable lithium plating and stripping during subsequent cycling (Fig. 7b,c). In a separate investigation, Zhang's research team explored atomically dispersed and lithiophilic CoN_x-doped carbon (CoNC) as a material conducive to uniform Li nucleation and deposition, where Li atoms are concurrently bonded to N and Co as shown in Fig. 7d [76]. The coordination between Co and N effectively governs the local electronic structure. In comparison to N sites in N-doped graphene, the CoN_x center, possessing heightened electronegativity, exhibits a more robust attraction to Li ions and a reduced nucleation overpotential. Consequently, the CoNC electrode exhibits a stable and high Coulombic efficiency of 99.2 % across nearly 400 cycles at 2.0 mA cm^{-2} and 350 cycles at 5.0 mA cm^{-2} (Fig. 7e).

Furthermore, other SA metals like Ni, Fe, or Cu, supported on MXene layers, have been investigated as hosts for lithium to promote nucleation and dendrite-free growth (Fig. 8a) [77]. Particularly, Zn-MXene was synthesized through a two-step ball-milling/pyrolysis process in an argon environment. The uniform distribution of N(Li) elements on Zn-MXene layers suggests that lithium tends to nucleate uniformly on Zn-MXene layers. This configuration of single zinc atoms immobilized on MXene layers efficiently stimulates Li nucleation and growth. In the initial plating stage, lithium tends to nucleate uniformly on the Zn-MXene layers' surface due to a significant presence of Zn atoms, followed by vertical growth along the nucleated sites due to a strong lightning rod effect at the edges, leading to bowl-like lithium deposition without dendrites. This design achieves a low overpotential of 11.3 ±

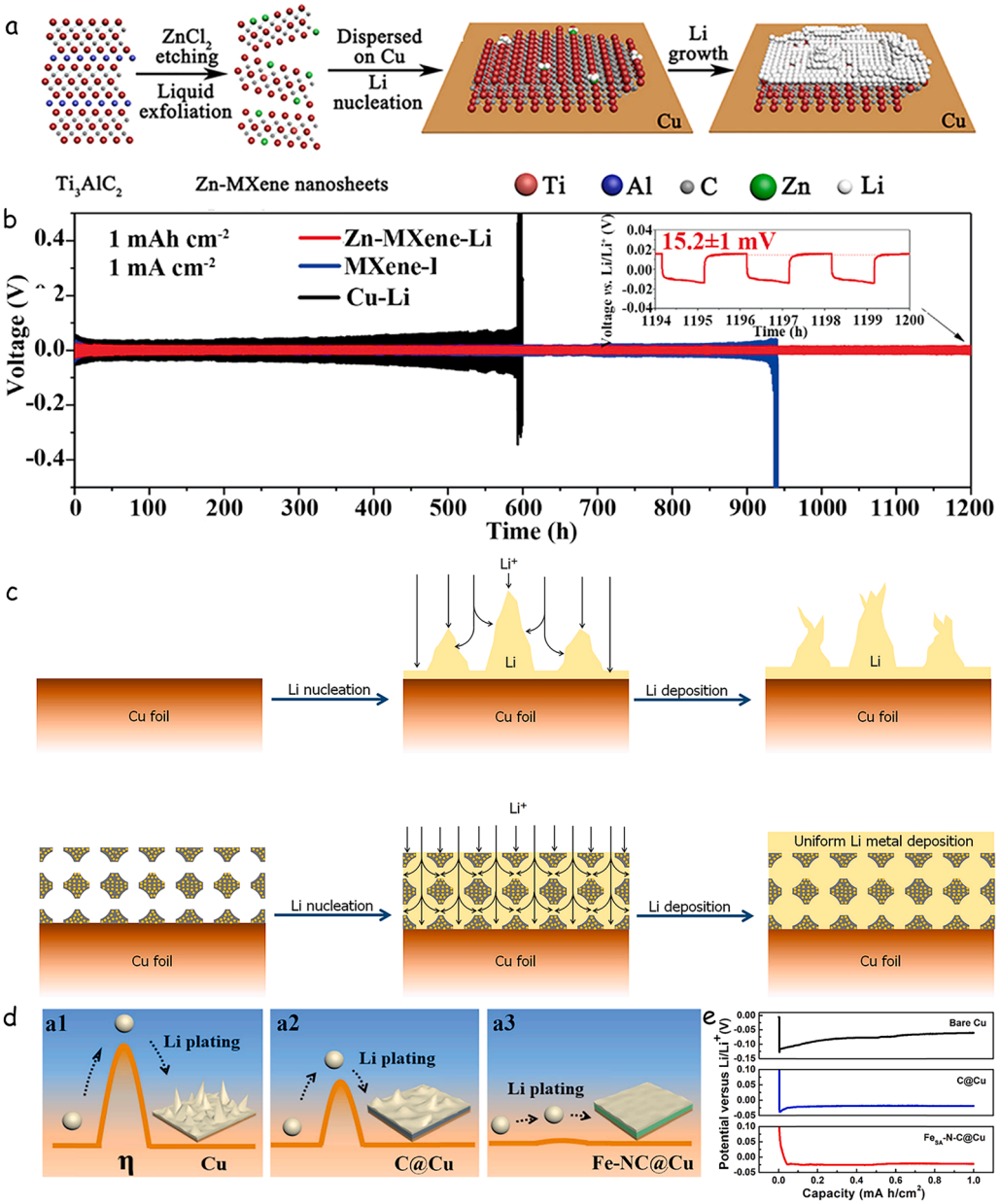

Fig. 8. (a) Synthesis process of Zn SA immobilized on MXene layers (Zn-MXene) for the Li nucleation and growth. (b) Cycle performances for symmetric cells with Zn-MXene-Li, MXene-Li, and Cu-Li anodes at 1 mAh cm^{-2}. Inset diagram is the selected stripping-plating curves of the Zn-MXene-Li anode. Reproduced with permission [77] Copyright 2021, Wiley-VCH. (c) Schematic illustration of Li nucleation and deposition process on Cu foil (top) and NOMC-Ni-coated Cu foil (bottom). Reproduced with permission [21] Copyright 2022, Wiley-VCH. (d) Schematic representation of the Li plating process on the Cu, C@Cu, and FeSA-N-C@Cu electrodes (η means the nucleus overpotential of the Li deposition). (e) Overpotential of Li nucleation and plating on bare Cu, C@Cu, and FeSA-N-C@Cu electrodes. Reproduced with permission [78] Copyright 2019, American Chemical Society.

0.1 mV, extended cyclic stability (1200 h), and deep stripping-plating capacities up to 40 mAh cm^{-2} using Zn-MXene films as lithium anodes (depicted in Fig. 8b).

In a separate study, Huang et al. demonstrated that a mesoporous carbon material, enhanced with nitrogen and featuring a three-dimensional interconnected pore structure with evenly distributed Ni lithiophilic sites (NOMC-Ni), significantly aids in the even nucleation and growth of lithium [21]. As illustrated in Fig. 8c, the NOMC-Ni material effectively facilitates the uniform distribution of lithium metal across its well-ordered mesoporous channels, hindering the formation of lithium dendrites. By utilizing the combined advantages of the 3D mesoporous design and the lithiophilic sites, the NOMC-Ni/Li electrode achieves a high Coulombic efficiency of 99.8 % over 200 cycles, coupled with a remarkably low initial potential for lithium nucleation. Additionally, when combined with commercial $LiFePO_4$ (LFP), the Li-NOMC-Ni||LFP configuration maintains a high capacity and average Coulombic efficiency. Beyond the aforementioned SAs, Fe SAs in an N-doped carbon matrix (FeSA-N-C) were prepared as lithiophilic sites to mitigate Li nucleation (depicted in Fig. 8d) [78]. FeSA-N-C catalysts exhibit a lower overpotential (0.8 mV) in comparison to a pristine carbon matrix (18.6 mV) due to the uniform deposition of Li on the electrode surface facilitated by SA Fe and N-doping of the carbon matrix, restraining the growth of Li dendrites (Fig. 8e). DFT studies highlighted the strong interaction between lithium ions and FeSA-N-C catalysts on an atomic scale. As a result, unlike the inconsistent Coulombic efficiency seen in plain Cu foil and C@Cu electrodes, the FeSA-N-C@Cu electrode achieves a Coulombic efficiency of 98.8 % across roughly 200 cycles. This indicates that FeSA-N-C catalysts improve lithium usage and inhibit dendrite formation in electrochemical reactions.

In sum, these studies validate the significant potential of SACs in safeguarding Li metal anodes. However, while modifying sulfur cathodes and cell separators have received substantial attention, fewer publications focus on enhancing Li metal anodes in LSBs. Thus, it is crucial to dedicate more research efforts to exploring the application of SACs for enhancing Li anode protection.

3.2. SAC-modified separator

The separator is an essential component of an LSB as it ensures stable operation and influences the electrochemical performance of the battery. Commercially available polyacrylonitrile separators with relatively large pores are commonly used in LSBs. While these large pores facilitate the transport of Li^+ ions, they also allow polysulfides dissolved in the electrolyte to move between the cathode and anode, negatively impacting the battery's cycling stability. To address this issue, separators modified with carbon-supported SAs have been developed to trap

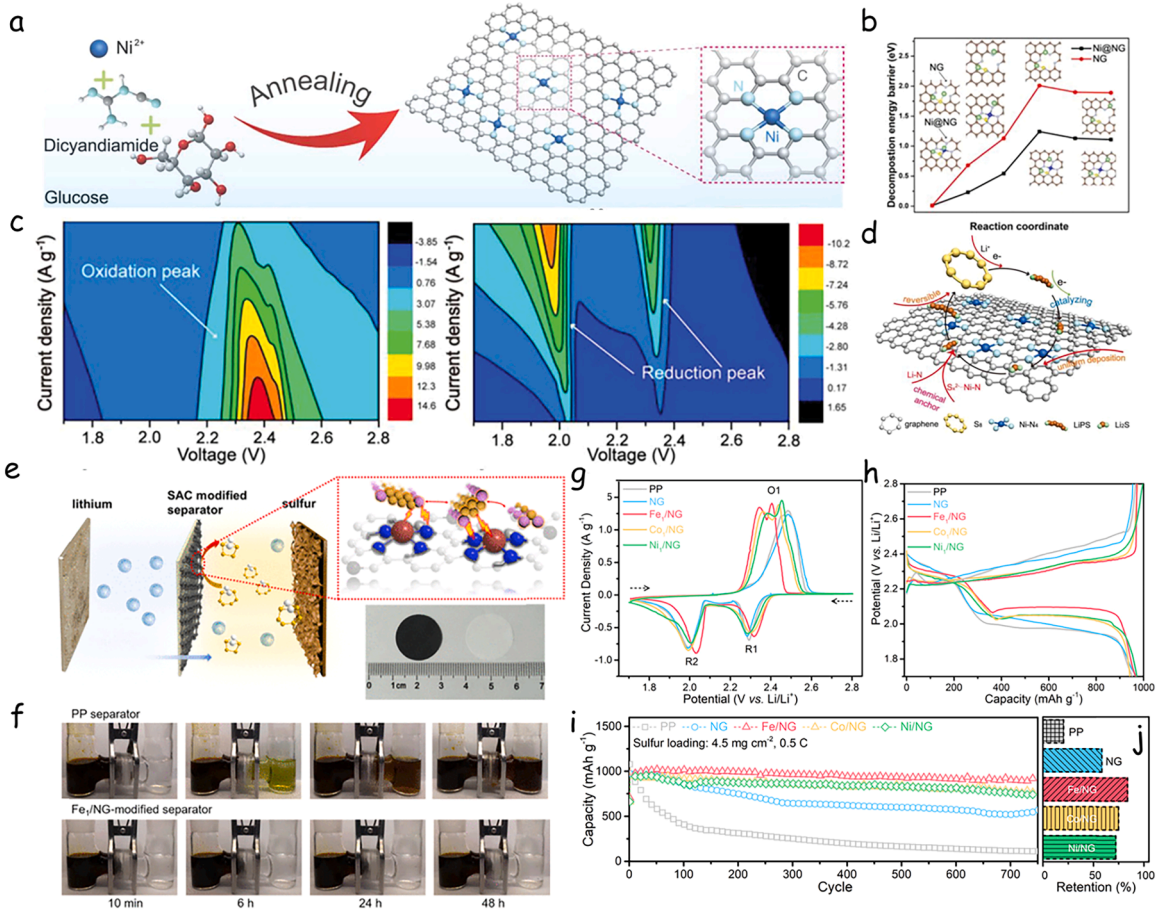

Fig. 9. (a) A diagram illustrating the synthesis processes involved in producing Ni-NG with the inclusion of Ni-N_4 sites. (b) Comparison of the decomposition energy barriers of Li_2S on both Ni-NG and NG surfaces. The blue, cyan, green, yellow, and brown spheres represent Ni, N, Li, S, and C atoms, respectively. (c) Cyclic voltammetry (CV) curves of LSBs employing the Ni-NG-modified separator, depicting variations in scan rates from 0.1 to 1.0 mV s^{-1}. (d) The catalytic mechanism of LiPS on the Ni-NG surface during the electrochemical process. Reproduced with permission [52] Copyright 2019, Wiley-VCH. (e) Depiction of the preparation process for the M/NG-modified separator, with M representing Fe, Co, or Ni. The inset showcases a digital photograph of both the commercial polypropylene (PP) and Fe/NG-modified separators. Additionally, a cross-sectional scanning electron microscope (SEM) image highlights the ultra-thin Fe_1/NG film on the PP membrane. (f) Results from polysulfide permeation tests comparing PP and Fe/NG-modified separators. (g) CV profiles of LSBs featuring unmodified PP, NG-modified separators, or M/NG-modified separators, at a scan rate of 0.1 mV s^{-1}. (h) Charge-discharge curves of LSBs operating at 0.5 C. (i) Performance trends of LSBs throughout cycling, and (j) corresponding capacity retention following 750 cycles. Reproduced with permission [72] Copyright 2019, American Chemical Society.

LiPS. The carbon layer in the modified separator acts as a physical barrier, preventing the diffusion of polysulfides towards the negative electrode, while the SA catalyst promotes the transformation of LiPS, enhancing the utilization of active materials.

In a study by Zhang et al. conducted a study involving Ni SAs on N-doped graphene (Ni-NG), prepared using a pyrolysis approach (Fig. 9a, b), and applied this material as a coating onto a separator using polyvinylidene fluoride (PVDF) as a binder [52]. The heightened catalytic efficacy of Ni-NG, validated through DFT calculations, showcased a reduced energy barrier during the conversion of LiPS. Calculations revealed that the decomposition energy barrier (1.23 eV) of Li_2S on the Ni-NG surface was notably lower compared to that on NG (1.98 eV). This lowered energy barrier facilitated efficient catalysis by the SA Ni on Ni-NG, accelerating the kinetics of delithiation during electrochemical processes [79–82]. Remarkably, even with a scan rate increase from 0.1 to 1.0 mV s^{-1}, the battery utilizing the Ni-NG-coated separator demonstrated two reversible redox peaks (Fig. 9c). The NG component offered excellent conductivity, maintaining the stability of isolated Ni SAs and facilitating swift electron transfer throughout the electrochemical process (depicted in Fig. 9d). The active Ni-N_4 centers present on Ni-NG effectively captured LiPS and catalyzed their kinetic conversion, thereby contributing to the enhanced electrochemical performance of LSBs.

In a subsequent investigation, Zhang et al. explored a modified commercial polypropylene separator integrated with graphene foam infused with various SACs (Fe, Co, or Ni, Fig. 9e) [72]. Among these metals, DFT calculations indicated that the Fe SAC exhibited the highest adsorption energy. The Fe-NG film, uniformly and densely applied onto

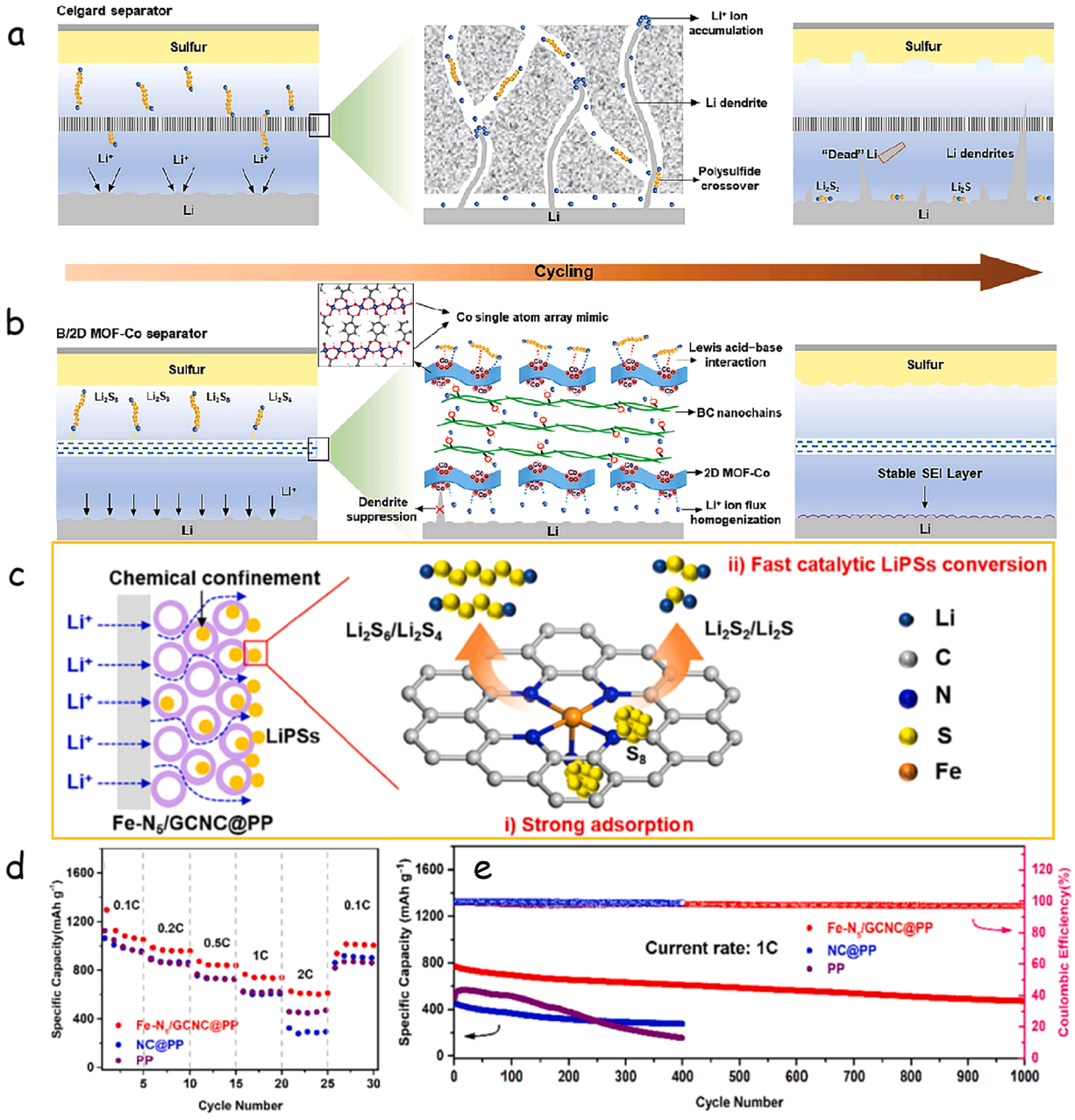

Fig. 10. Comparative schemes of LSBs with different separators. (a) Non-active Celgard membrane showing growth of Li dendrites and migration of LiPSs. (b) Active B/2D MOF-Co membrane adsorbing LiPS and regulating Li^+ deposition and growth. Reproduced with permission [85] Copyright 2020, Wiley-VCH. (c) Chemical confinement and catalytic conversion mechanism of a Fe-N_5/GCNC@PP separator. (d) Rate performance of Li-S cells with various separators. (e) Cycling performances of LSBs with different separators. Reproduced with permission [87] Copyright 2023, Elsevier.

the polypropylene separator, maintained a thickness of around 7 μm while preserving robust stability and mechanical durability despite repeated bending and wrinkling. The ability of these modified separators to adsorb LiPS was verified through adsorption and permeation experiments, demonstrating that LiPS remained non-dissolved in the Fe-NG-based separator even after 48 h (Fig. 9f). Electrochemical assessments of LiPS redox chemistry showcased an improved LiPS redox kinetics from the separator. As shown in Fig. 9g, the two cathodic peaks account for the reduction of sulfur into LiPS (Li_2S_x, peak R1) and their subsequent conversion to solid-state Li_2S_2/Li_2S (peak R2). Besides, the anodic peak (peak O1) is associated with the conversion of Li_2S to LiPS and subsequently to sulfur. It can be seen that Fe_1-NG-modified separator displayed a more positive potential of cathodic peaks and a more negative anodic peak than Ni_1-NG and Co_1-NG-modified separator. Therefore, the introduction of Fe-NG electrocatalysts onto the separator led to a reduced voltage gap and enhanced current density, indicating ameliorated reaction kinetics for polysulfide reactions [83,84]. Batteries employing the Fe_1-NG-modified separator were characterized by improved specific capacities compared to those using polypropylene, NG-modified, or other SA-NG-modified separators (Fig. 9h). Even after prolonged cycling at 0.5 C, the Fe-NG-based battery exhibited notably superior capacity retention (83.7 %) compared to NG-based (58.3 %), Ni-NG-based (72.1 %), Co-NG-based (74.8 %), and polypropylene-based (20.4 %) batteries (Fig. 9i,j). The improved cycling performance of the Fe-NG-based battery could be attributed to the presence of individual Fe atoms, which effectively reduced the presence of LiPS in the electrolyte and enhanced the utilization of LiPS. As observed in this work, compared with other metals, Fe SACs can act as particularly effective regulators in sulfur electrochemistry suppressing the migration of LiPSs and accelerating the bidirectional sulfur redox kinetics.

Guo and coworkers demonstrated the advantageous utilization of Co SACs in ameliorating the LiPS conversion at the cathode and the lithium plating/stripping processes at the anode within LSBs [85]. Their work involved the fabrication of a self-standing separator by combining SA Co MOF with bacterial cellulose (BC, Co-MOF/BC). The effects of this separator were assessed in comparison with conventional separators (Celgard and BC) in typical Li-S cells. The results illustrated in Fig. 10a,b showcased the evolution of active sulfur and lithium metal in Li-S cells employing Celgard and B/2D MOF-Co separators. When Celgard was used as the separator, soluble LiPS generated at the cathode could easily traverse the porous separator and react with the lithium metal anode, resulting in the formation of insoluble and insulating lithium sulfides (Li_2S_2 and Li_2S) on the anode surface. This hindered the active sulfur content and caused increased polarization due to lithium anode surface passivation. Additionally, inhomogeneous lithium plating and stripping led to the formation of dendritic lithium structures, increasing side reactions with the electrolyte and raising internal resistance. Furthermore, lithium dendrites could penetrate the separator and cause internal short circuits, posing safety risks. In contrast, the introduction of the bifunctional B/2D MOF-Co separator effectively curtailed the LiPS shuttling effect and lithium dendrite growth. The Co-O_4 moieties present on the 2D MOF-Co nanosheets captured polysulfides through Lewis acid-base interactions, promoting uniform lithium-ion flux by adsorbing Li^+ ions on surface O atoms [86]. The high Young's modulus of the B/2D MOF-Co separator acted as a robust physical barrier against lithium dendrite growth. Cells equipped with the Co-MOF/BC separator exhibited superior capacities across various current rates compared to those with conventional separators. Scanning electron microscopy (SEM) analysis of the cycled cell illustrated the separator's stable surface, and the lithium anode displayed a dendrite-free surface. Moreover, stable lithium plating and stripping were observed in symmetric and asymmetric Li cells employing Co-MOF/BC separators. Its potential applicability in flexible pouch cells was validated under diverse bending conditions. The atomic model configuration highlighted the formation of S-Co and Li-O bonds between the Co-MOF and sulfur species, reinforcing the Co-MOF's ability to capture LiPS.

Additionally, He et al. innovated a functional separator, integrating graphitic carbon nanocapsules (GCNC) with a Fe SAC (Fe-N_5/GCNC@PP) produced through high-temperature carbonization [87]. The separator showed high LiPS chemical affinity and superior catalytic activity, inhibiting the LiPS migration to the anode and accelerating their conversion (Fig. 10c). Thus, LSBs based on the Fe-N_5/GCNC@PP separator provided significantly improved rate performance and cycling stability, as depicted in Fig. 10d,e.

In conclusion, the integration of highly active SACs in LSB separators effectively counteracted LiPS diffusion and enhanced LiPS conversion kinetics, thereby mitigating the LiPS shuttle effect. These SACs also regulated lithium plating and stripping, hindering lithium dendrite growth. This holistic enhancement of both sulfur cathode and lithium anode attributes contributes to optimizing battery performance.

3.3. SAC-decorated cathodes

In the context of LSBs, the cathode is constructed using solid sulfur as the active material, and a carbon host is employed to amplify electrical conductivity. Carbon materials exhibiting exceptional conductivity, a well-suited distribution of pore sizes, and a significant specific surface area emerge as prime candidates for effectively sequestering sulfur and facilitating the interconversion of Li_2S_2/Li_2S. Aiming to counteract the LIPs shuttle effect, researchers have formulated strategies such as spatial encapsulation, wherein techniques of physical containment are harnessed to mitigate the migration of sulfur species within the battery's architecture [88–92]. Additionally, investigators have delved into the amalgamation of polar materials, encompassing oxides and sulfides, with carbon hosts. This innovative approach capitalizes on chemical adsorption mechanisms and the establishment of catalytically active sites dedicated to LiPS. These measures effectively hinder the undesirable migration and reactions of LiPS [93–98]. However, despite these persistent efforts, the catalytic efficiency limitations and suboptimal electrical conductivity inherent to catalysts composed of metal oxides/sulfides continue to impede the attainment of superior electrochemical performance within LSBs. Consequently, the incorporation of SACs endowed with heightened catalytic activity becomes a paramount requirement, poised to further amplify the comprehensive electrochemical performance of LSBs. This imperative for augmented catalysis

Table 1
Summary of recent reports on SACs-based materials for LSBs.

Catalysts	Capacity (mAh g^{-1}) (current rate)	(cycles, current rate, decay rate))	Category	Mass loading of SACs	Ref.
Fe-N/MHCS	1110 (0.2 C)	(1000, 1 C, 0.0187 %)	Host	1.03 wt %	[46]
Fe-N_5-C	1170 (0.2 C)	(500, 1 C, 0.054 %)	Host	0.02 wt %	[102]
Mo–N_2/C	1300 (0.1 C)	(550, 2 C, 0.018 %)	Host	0.36 wt %	[104]
Co-CMP	1404 (0.1 C)	(1000, 0.5 C, 0.045 %)	Host	2.32 wt %	[105]
Co–SAs@NC	1438 (0.1 C)	(600, 1 C, 0.046 %)	Host	0.66 wt %	[107]
CoSA-N-C	1574 (0.05 C)	(1000, 1 C, 0.035 %)	Host	15.3 wt %	[109]
SAV@NG	1143 (0.2 C)	(400, 0.5 C, 0.073 %)	Host	4.3 wt %	[110]
ZnN_4-NC	1225 (0.2 C)	(500, 5 C, 0.032 %)	Host	8.3 wt %	[111]
Ni-N_5/HNPC	1188 (0.2 C)	(500, 0.5 C, 0.053 %)	Host	0.6 wt %	[112]
Fe_1/NG	1200 (0.2 C)	(750, 0.5 C, 0.021 %)	Separator	0.57 wt %	[72]
B/2D MOF-Co	1138 (0.1 C)	(600, 1 C, 0.070 %)	Separator	24.8 wt %	[85]
SA-Fe@NG	1117 (0.2 C)	(200, 0.2 C, 0.097 %)	Separator	1.33 wt %	[113]

is underscored by the necessity to enhance the efficiency of LSBs, a fact substantiated by the insights presented in Table 1.

Shao et al. introduced a Fe SAC nanoreactor (Fe-N/MHCS) for sulfur utilization in LSBs [46]. Utilizing XAS, they confirmed the presence of Fe atoms within Fe-N/MHCS and unveiled the intricate role of Fe-N_4 centers as multi-effect catalytic sites, facilitating the conversion of LiPS, deposition of Li_2S, and decomposition processes. Through a LiPS adsorption experiment coupled with UV–vis absorption spectroscopy, they monitored the concentration shift in a Li_2S_6 solution upon introducing MHCS, N/MHCS, and Fe-N/MHCS samples. The characteristic absorption peak at around 420 nm, corresponding to Li_2S_6, diminished for MHCS and N/MHCS samples, and entirely vanished for the Fe-N/MHCS variant, indicating robust chemisorption between Fe-N_4 sites and LiPS (Fig. 11a) [99–101]. To delve into the electrocatalytic effect of Fe-N/MHCS, theoretical computations involving reactant adsorption and other parameters were carried out. These calculations explored the binding geometries of soluble long-chain LiPS molecules interacting with Fe-N_4 or N-doped sites to achieve the lowest system energy. As depicted in Fig. 11b, the results vividly displayed that positive Fe atoms and negative N atoms within Fe-N_4 sites form "Fe-S" and "Li-N" bonds with S and Li atoms in LiPS molecules atop the Fe-N_4-C substrate. In contrast, solely Li-N bonds are observed on the N-C substrate. Consequently, Fe-N_4 sites, characterized by lithiophilic and sulfiphilic traits derived from Lewis acid-base interactions, exhibit a more potent chemisorptive affinity towards LiPS [102,103]. Additional theoretical calculations were carried out to assess the Gibbs free energies at various stages of the sulfur reduction process on Fe-N_4-C and N-C substrate surfaces. As shown in Fig. 11c, the Gibbs free energy for reducing solid-state Li_2S_2 to solid-state Li_2S decreases from 0.82 eV on N-C substrates to 0.59 eV on Fe-N_4-C substrates. This highlights the role of Fe-N_4 centers in promoting LiPS conversion to Li_2S. Besides, the energy barriers for the decomposition of Li_2S during oxidation on Fe-N/MHCS and N/MHCS were also evaluated. As illustrated in Fig. 11d, e, the Fe-N_4-C site notably lowers the decomposition barrier of Li_2S (1.43 eV), significantly surpassing that of the N-C substrate (1.84 eV). This underscores the favorable impact of Fe-N_4 active sites in catalyzing Li_2S oxidation. Consequently, the Fe-N_4-incorporated Fe-N/MHCS nanoreactors, boasting high specific energy and prolonged LSB lifespans, exhibit several advantages (Fig. 11f). Firstly, the MHCSs, endowed with ample mesoporous architectures, can accommodate substantial sulfur loads, mitigate volume fluctuations, establish effective pathways for electrons and ions, and ensure uniform dispersion of single Fe atoms. Secondly, the Fe and N atoms within atomically dispersed Fe-N_4 centers function as Lewis acidic and basic sites, facilitating the robust binding of S and Li atoms in LiPS molecules via "Fe-S" and "Li-N" bonds. Thirdly, the Fe-N_4 active center, operating as a multi-effect electrocatalyst, adeptly catalyzes LiPS redox reactions, Li_2S precipitation, and dissociation processes. This effectively curtails the notorious shuttle effect, enhances Li_2S utilization, and boosts cycling stability. Leveraging these strengths, the Fe-N/MHCS nanoreactors, meticulously designed at the atomic level, serve as novel sulfur hosts, culminating in high specific energy and long-lasting cycling stability, even within cells featuring high areal sulfur loading and low electrolyte-to-sulfur (E/S) ratios.

In addition to SA Fe catalysts, SA Co has also undergone extensive exploration as a catalyst in LSB cathodes [105,106]. Li et al. pioneered the synthesis of N-doped carbon dodecahedra-supported Co SAs (Co-SAs@NC) as sulfur hosts, achieved through the pyrolysis of a Co-Zn MOF precursor (Fig. 11g) [107]. The inclusion of Zn in the precursor served a dual purpose: firstly, it occupied specific coordination sites of Co, facilitating the even dispersion of atomic Co; secondly, it generated

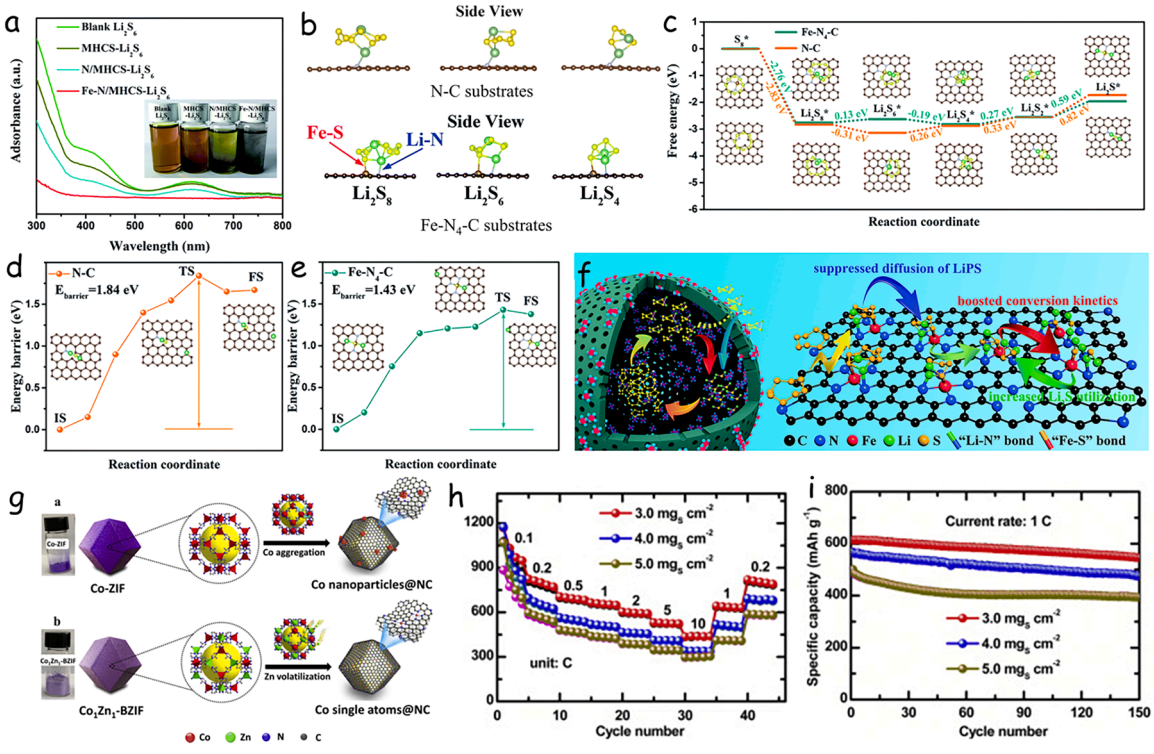

Fig. 11. (a) UV–vis spectra of Li_2S_6 solution after 2 h with the addition of different adsorbents (inset: Li_2S_6 solutions after 2 h). (b) Calculated configurations of polysulfides on the Fe-N_4-C and N-C substrates with the lowest system energies. (c) Energy profiles for sulfur reduction on N-C and Fe-N_4-C substrates (inset in c: optimized adsorption configurations). Energy profiles for Li_2S cluster dissociation on (d) N-C and (e) Fe-N_4-C substrates (insets in d and e: initial, transition, and final states denoted as IS, TS, and FS). Green, yellow, silver, and brown balls represent Li, S, N, and Fe atoms, respectively. (f) Schematic illustration of Fe-N_4 embedded Fe-N/MHCS nanoreactors as electrocatalysts for sulfur cathodes. Reproduced with permission [46] Copyright 2020, Royal Society of Chemistry. (g) Schematic illustration of synthesis processes for (a) Co nanoparticles and (b) Co SAs supported on nitrogen-doped carbon. (h) Rate performance from 0.1 to 10 C, and (i) cycle life of S@Co-SAs@NC with different areal sulfur loadings: 3.0, 4.0, and 5.0 mg cm^{-2}. Reproduced with permission [107] Copyright 2020, Elsevier.

vacancies for N atoms upon the selective evaporation of Zn. Computational analysis using DFT revealed that the adsorption energy of Li_2S and Li_2S_6 on Co-SAs@NC was notably lower (-1.59 and -2.36 eV) compared to their adsorption on the Co (111) surface (-4.18 and -8.67 eV). Despite this discrepancy, the Co-SAs@NC cathodes exhibited superior performance in terms of rate capability and recyclability. This phenomenon can be attributed to the partial surface sulfurization of cobalt nanoparticles, resulting in an irreversible depletion of active sulfur due to the robust adsorption capacity of the Co (111) surface towards Li_2S and Li_2S_6. A similar degradation of Li-S bonds and disintegration of Li_2S_n species has been observed in specific high adsorption capacity 2D layered materials like V_2O_5. Leveraging the substantial adsorption capability of catalytic Co-SAs@NC, the researchers achieved a remarkable capacity of 300 mAh g^{-1} at 10C, maintaining prolonged cycling stability with minimal capacity degradation. Notably, the material demonstrated consistent performance over 150 cycles at 1 C, even under high sulfur loading conditions (5.0 mg cm^{-2}) (Fig. 11h,i).

Furthermore, Du and co-researchers elucidated that Co-N/G significantly expedited the conversion of LiPS [57]. Employing XAS and first-principle calculations, they unveiled the Co-N-C coordination center's role as a bifunctional electrocatalyst, facilitating the formation and breakdown of Li_2S during discharge and charge processes, respectively. This insight led to the achievement of an areal capacity of 5.1 mg cm^{-2} at 0.2 C in S@Co-N/G electrodes with a high sulfur loading of 6.0 mg cm^{-2}, while maintaining a stable performance with a capacity decay rate of 0.029 % per cycle over 100 cycles. Wu et al [55] introduced Co SACs onto C_3N_4, yielding a substantial specific capacity of approximately 1400 mAh g^{-1} at 1.6 mA cm^{-2} for the Co SACs-based cathode. Even with 4 mg cm^{-2} of sulfur, the cycling stability at 2 mA cm^{-2} was sustained for 200 cycles, maintaining a capacity of around 780 mAh g^{-1}. Prior reports have highlighted the typically low content of SACs in the matrix material (usually < 5 wt %) [52]. To bolster battery performance, researchers aimed to incorporate a significant number of active sites within the matrix material to support SACs [108]. Li et al. employed a salt template method to create N-doped carbon nanosheets with SA Co incorporation, achieving a Co content of up to 15.3 wt %. The dense Co-N_4 coordination center acted as a catalytic site, facilitating the reversible conversion between LiPS and Li_2S. Additionally, the CoSA-N-C material facilitated the uniform deposition of Li_2S nanoparticles and catalyzed Li_2S oxidation. Consequently, the CoSA-N-C@S electrode exhibited a high specific capacity of 624 mAh g^{-1} at 5 C and a fading rate of 0.035 % per cycle over 1000 cycles at 1 C [109]. In summary, both experimental and computational findings unequivocally demonstrate that incorporating SACs into the cathode substantially enhances LSB performance. This integration enhances the adsorption of soluble LiPS and reduces the energy barriers related to delithiation and interconversion reactions, ultimately improving sulfur utilization, rate capabilities, and the overall lifespan of LSBs.

SACs based on 3d metals strongly bind LiPS, limiting LIPS migration and contributing to their dissociation by weakening the neighboring Li-S bonds [114–116]. According to Han et al., the activity of different metallic SACs can be evaluated from the metal-sulfur d-p orbital hybridization (Fig. 12a) [117]. Among the different 3d elements, Ti displays particularly effective d-p hybridization, tightly binding to S

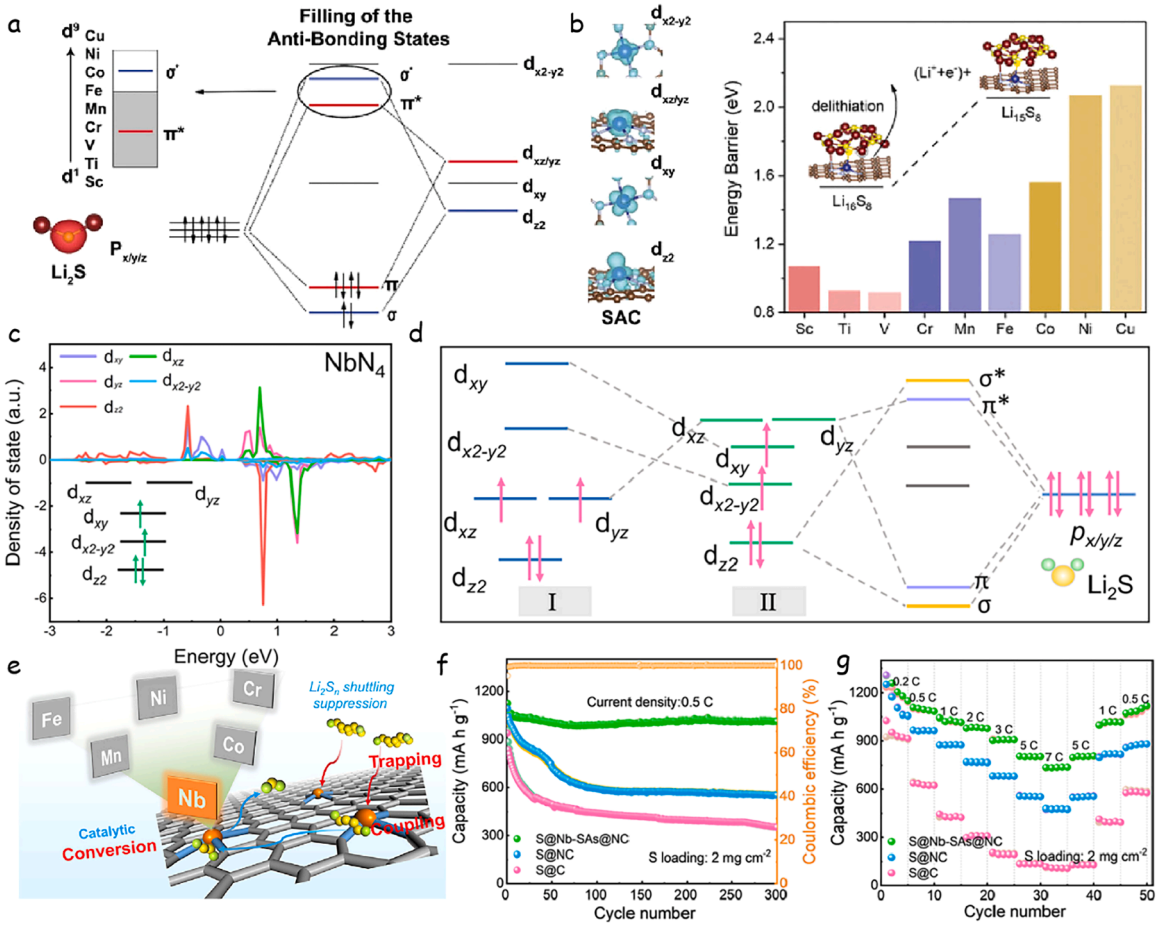

Fig. 12. (a) Scenario of d-p orbital hybridization between SACs and Li_2S. (b) The delithiation energy barrier during the $(Li_2S)_8$ oxidation process. Reproduced with permission [117] Copyright 2021, Wiley-VCH. (c) PDOS of Nb-d orbital. (d) Spatial charge density for SANb and Li_2S, exhibiting the typical d-orbital and p-orbital distribution pattern. (e) Schematic illustration of polysulfide adsorption on M-SAs@NC (M = Nb, Cr, Mn, Fe, Co, and Ni). (f) Cycling performance, and (g) Rate performance of S@Nb-SAs@NC cathodes. Reproduced with permission [118] Copyright 2023, American Chemical Society.

(Fig. 12b). Zhang et al. compared the performance of several transition metal SACs (M-SAs@NC) towards the LIPS conversion, by detailed analysis of their electronic structure [118]. They found the M-SAs@NC d_{z2} and $d_{xz/yz}$ orbitals to be more stable for square planar coordination of D_{4h} symmetry. Comparing the different metals, Nb SACs in the optimized NbN_4 geometry showed particular features increasing the $d_{xz/yz}$ and d_{z2} orbitals while reducing d_{xy} and $d_{x2\text{-}y2}$ (Fig. 12c,d). Thus, while d_{xz} and d_{yz} orbitals are empty in Nb SACs, d_{z2}, d_{xy}, and $d_{x2\text{-}y2}$ appear filled. When moving from Nb to Ni, antibonding (π* and σ*) states are gradually occupied and the energy gap between the bonding (π and σ) and antibonding (π* and σ*) states progressively decreases, which weakens the binding strength. Overall, among the different metals, Nb SACs demonstrated superior LiPS binding capability and enhanced kinetics of the sulfur redox reactions (Fig. 12e), which contributed significantly to boosting the cell cycling stability (Fig. 12f,g).

Despite the success of SACs in promoting the sulfur redox kinetics, high SA loads can lead to SA migration and clustering, thus reducing the density of active sites and diminishing the catalyst performance. Due to this loading limitation, when a reaction involves the activation of two or more reaction molecules, its catalytic activity is often inhibited to a certain extent due to the lack of sufficient catalytically active sites. The SAs content in the currently reported SACs is typically below 3 wt %. This low amount suggests a scarcity of atomic active sites for the catalytic conversion of polysulfides, which is a notable limitation for the efficient catalytic conversion of polysulfides. This limitation becomes especially critical under conditions of high sulfur loadings, lean electrolyte amounts, and high charge/discharge rates that are essential for the commercial viability of LSBs. Therefore, developing SACs with more active sites is fundamental. To this end, dual-metal SACs and even tripel-metal SACs composed of two or three different metal SAs have emerged as a new class of catalysts showing great potential for application in different electrochemical technologies, including LSBs [119–121]. In this direction, Ma et al. synthesized N-coordinated Fe and Co binary metal SACs on a hierarchical porous carbon (Fe/Co-N-HPC) and evaluated its performance as a cathode catalytic additive (Fig. 13a). Compared with the Fe SAC, the dual Fe/Co SAC exhibited promoted ability towards polysulfide conversion associated with the higher electronic density achieved in Fe sites with the presence of Co (Fig. 13b,c). Thus, LSBs based on the Fe/Co-N-HPC displayed improved rate capability, long-term cyclic stability, and areal capacity (Fig. 13d,e).

In a similar direction, Yang et al. developed a Fe/V dual SAC (Fe/V-N_7) on a carbon support (DAC). This catalyst was inspired by the Fe/V centers in N/S fixation bioenzymes. Like in the Fe/Co SAC, in the Fe/V SAC V is also found to regulate the electronic population of the Fe 3d orbitals. The strong coupling between Fe/V 3d and S 2p orbitals promoted the LIPS anchoring and conversion, overall boosting the kinetics of the Li-S reaction (Fig. 13f,g). Consequently, the obtained LSBs presented strongly improved cycling stability and rate capability (Fig. 13h).

4. Conclusions and perspectives

High-energy density and long-lasting LSBs exhibit potential for the implementation of energy storage systems. Nevertheless, there exist prevalent challenges associated with Li anodes and sulfur cathodes, including the occurrence of Li dendrites, rupture of the SEI film, volumetric variations during the process of Li plating and stripping, LiPS migration, and incomplete sulfur utilization. To tackle these challenges, it is imperative to utilize materials that possess exceptional

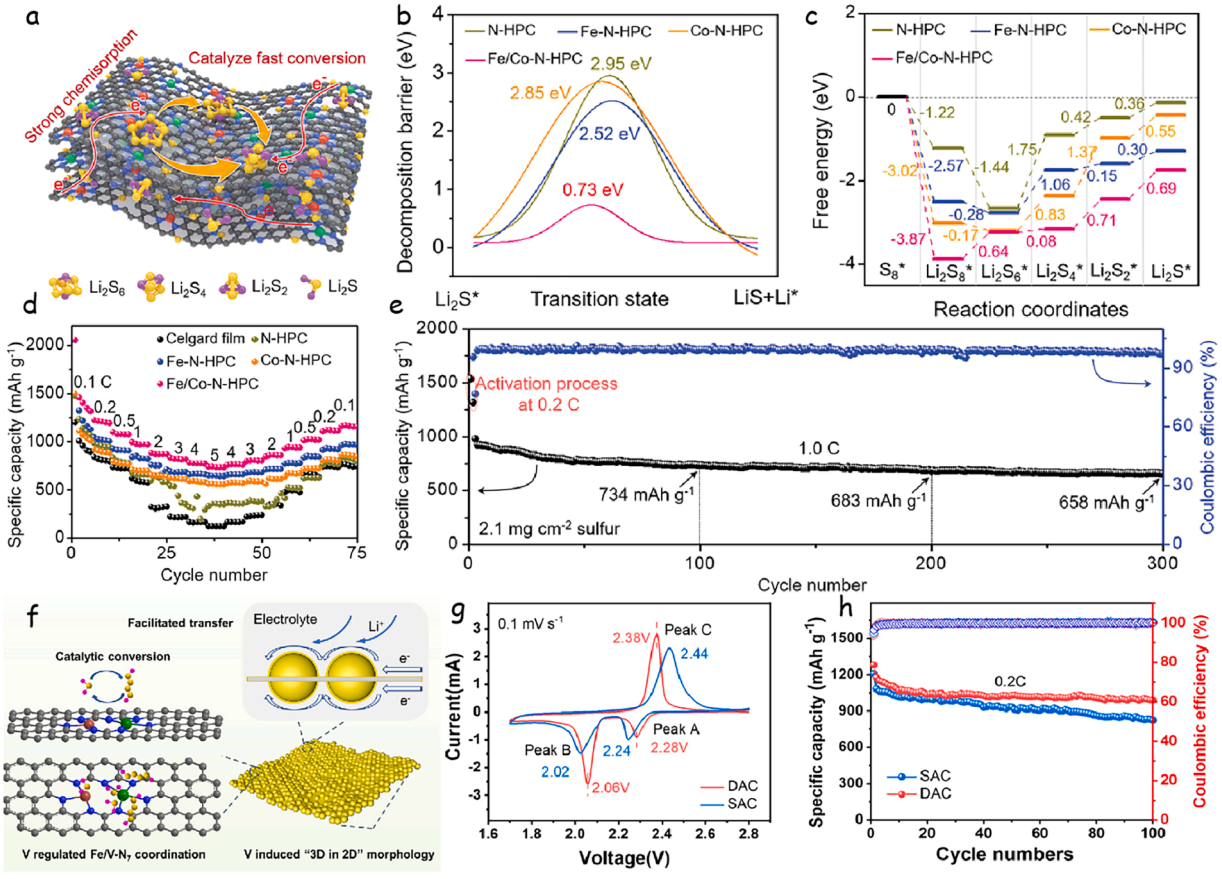

Fig. 13. (a) Catalysis mechanisms of Fe/Co-N-HPC in LSBs. (b) Decomposition barriers of Li_2S on different catalysts. (c) The calculated free energy values of the discharge process from S_8 to Li_2S on different catalysts. (d) Rate performance from 0.1 to 5 C, and (e) cycle life of LSBs based on the Fe/Co-N-HPC materials with high areal sulfur loading. Reproduced with permission [119] Copyright 2022, Wiley-VCH. (f) Schematic illustration of the mechanism for sulfur conversion on DAC. (g) CV curves, and (h) cycling performance of different electrodes. Reproduced with permission [122] Copyright 2023, American Chemical Society.

lithiophilicity, a strong affinity for LiPS, and demonstrate catalytic activity. SACs have gained significant popularity in the field of LSBs due to their ability to fulfill the necessary criteria and serve as versatile components, including sulfur host materials, interlayers, and separators. To gain a deeper comprehension of the functioning of SACs in LSBs, a thorough analysis of recent advancements in this field has been undertaken. This encompasses the examination and discourse of the mechanism of action, along with the variables that influence the activities and preparation methodologies of SACs.

SACs are of paramount importance in expediting phase-transfer reactions and impeding the migration of LiPS and the formation of lithium dendrites. These effects ultimately result in enhanced Coulombic efficiency and prolonged cyclability. The utilization of SACs with a high density of lithiophilic sites has been found to effectively decrease the nucleation overpotential during the application of lithium metal anodes. Moreover, the inherent activity of SACs facilitates the diffusion of lithium ions and the conversion of sulfur species. The inherent flexibility of SACs effectively addresses the issue of volume fluctuations in both the lithium anode and sulfur cathode that occur as a result of repeated charge and discharge cycles. Furthermore, the capacity of SACs to adsorb LiPS serves to mitigate the depletion of active sulfur materials and improve overall utilization efficiency. Additionally, when used as separator and interlayer components, lightweight SACs decrease the overall battery mass, thus increasing energy density. On top of these, dual-function separators can simultaneously inhibit Li dendrite formation and the shuttle effect of LiPS.

However, despite their demonstrated interest and the significant progress in the development of SACs for LSBs, there are still obstacles that hinder future advancements in this field.

(1) Synthesizing stable and high-metal-loading SACs poses a significant challenge due to the elevated potential for agglomeration, arising from the substantial surface energy of individual metal atoms. This can result in a limited mass loading of SAs, leading to insufficient active sites and potential setbacks in their practical implementation in LSBs. Too high SA concentrations result in their aggregation and thus the loss of their catalytic properties. While the SA content is generally limited to below 3 %, higher SA concentrations above 5 wt % are desirable to promote performance, especially in high sulfur loading and lean electrolyte conditions and when targeting high charge/discharge rates. Consequently, it becomes crucial for forthcoming research endeavors to focus on devising straightforward and cost-effective synthetic methodologies that enable the creation of SACs with high loadings. These synthetic strategies should be also scalable to enable the industrial production of these materials to cope with the potential high demands of future LSBs. Moreover, these synthetic pathways should ensure the SACs' durability under operational conditions to counteract the tendency of metal atoms to aggregate during charge/discharge cycles, which could otherwise compromise electrochemical stability. A step forward in this direction could be the use of binary and even ternary SACs as those recently emerging in the LSB field and others.
(2) For preparing SAs on carbon-based substrates, the selection of metal sources and organic ligands plays a pivotal role in shaping the microscopic coordination environment. The configuration of SACs should extend beyond the recognized Fe-N-C and Co-N-C sites. Coordination with other elements should be investigated to promote the catalyst activity. These investigations have the potential to guide modifications to significant yet limited active sites. Furthermore, the incorporation of multiple metal centers, including nonmetal centers, and the integration of diverse coordination components from varied supports (oxides, sulfides, selenides, etc.) or heteroatom doping represent noteworthy strategies. The presence of multimetal sites within SACs offers increased prospects for catalyst bifunctionality, exemplified by applications like ORR/OER processes in rechargeable Zn-air batteries.
(3) To attain a more comprehensive comprehension of the electrochemical mechanisms exhibited by SACs in rechargeable batteries, it is essential to conduct combined *in situ* and ex situ characterizations, augmented by theoretical calculations. An illustrative approach is the application of *in situ* TEM techniques, which can be employed to meticulously explore the structural transformations within the cathode and anode materials in the presence of SACs. Furthermore, the utilization of *in situ* XRD can give insights into the phase structural alterations occurring during charge/discharge sequences. Through DFT calculations, an in-depth understanding of the LiPS adsorption/desorption in the presence of SACs can be achieved. Hence, the combined application of *in situ* characterizations and DFT calculations can provide a clear understanding of the reaction mechanisms facilitated by SACs.
(4) While most current work on the use of SACs to enhance LSBs performance focuses on liquid electrolytes, polymer, and polymer-based composite electrolytes find advantages in mitigating Li dendrite formation, preventing LiPS migration, and reducing the risk of fire posed by some organic liquid electrolytes. Thus, the exploration of SAC performance on LSBs based solid electrolytes should be urgently undertaken.
(5) Although SACs hold great promise in enhancing the specific energy and cycling durability of LSBs, their eventual commercialization requires careful consideration of critical factors, including active material mass and the ratio of electrolyte to sulfur. Presently, extending the cycling longevity of LSBs often involves a compromise with energy density. This trade-off is accomplished through strategies such as reducing sulfur loading, elevating the electrolyte/sulfur ratio, and introducing an excess of lithium metal. To simultaneously achieve low lithium metal content, high sulfur loading, and a diminished electrolyte/sulfur ratio, the integration of SACs with highly conductive matrices and exceptional activity becomes crucial.

Collectively, SACs' unique catalytic attributes, robust adsorption capabilities, and lithiophilic nucleation sites offer significant paths to overcome limitations linked to the intrinsic behavior of redox-active LiPS and lithium metal. This, in turn, can pave the way for the advancement of LSBs towards successful commercialization.

The implementation of SACs in LSBs has demonstrated notable enhancements in both specific energy and cycling durability. However, the prospective commercialization of this technology necessitates careful consideration of crucial factors such as the mass of active materials and the ratio of electrolyte to sulfur. At present, the attainment of extended cycling lifetimes in LSBs frequently necessitates a trade-off in energy density. This trade-off is achieved by diminishing the S loading, augmenting the electrolyte-to-sulfur (electrolyte/S) ratio, and introducing surplus Li metal. To attain a reduced amount of Li metal, an increased S loading, and a decreased electrolyte/S ratio, there is a strong preference for SACs that possess highly conductive matrices and exhibit exceptional catalytic activity. In a comprehensive context, the diverse catalytic characteristics, notable adsorption capabilities, and lithiophilic nucleation sites inherent in SACs present considerable potential in addressing the limitations associated with the intrinsic attributes of redox-active LiPS and lithium metal. As a result, this has the potential to facilitate the advancement and eventual commercialization of LSBs.

CRediT authorship contribution statement

Dawei Yang: Conceptualization, Data curation, Funding acquisition, Writing – original draft, Writing – review & editing, Formal analysis. **Canhuang Li:** Data curation, Software, Writing – original draft, Writing – review & editing. **Meenu Sharma:** Data curation, Supervision, Writing

– review & editing. **Mengyao Li:** Data curation, Writing – review & editing, Conceptualization. **Jiaao Wang:** Data curation, Investigation, Writing – review & editing. **Jishi Wei:** Conceptualization, Data curation, Supervision, Writing – review & editing. **Kun Liu:** Data curation, Writing – review & editing. **Yizhou Zhang:** Conceptualization, Data curation, Writing – original draft, Writing – review & editing. **Junshan Li:** Formal analysis, Writing – review & editing. **Graeme Henkelman:** Formal analysis, Writing – review & editing. **Qiaobao Zhang:** Conceptualization, Data curation, Funding acquisition, Writing – original draft, Writing – review & editing. **Andreu Cabot:** Conceptualization, Data curation, Formal analysis, Funding acquisition, Writing – original draft, Writing – review & editing.

Declaration of competing interest

The authors declare that they have no known competing financial interests or personal relationships that could have appeared to influence the work reported in this paper.

Acknowledgments

D. Yang and J. Wei thank the China Scholarship Council for the scholarship support and the funding from the National Natural Science Foundation of China (NSFC) (Grants No. 22305064, 22308086). This project has received funding from the European Union's Horizon 2020 research and innovation program under grant agreement No 823717 – ESTEEM3. This work was financially supported by the National Natural Science Foundation of China (Grants Nos. 52122211, 52072323), the Frontier Exploration Projects of Longmen Laboratory (Grant No. LMQYTSKT008). Q. Zhang acknowledges the support of Nanqiang Young Top-notch Talent Fellowship in Xiamen University. A. Cabot acknowledges support from the 2BoSS project of the ERA-MIN3 program with the Spanish grant number PCI2022–132985/AEI/10.13039/501100011033, from Generalitat de Catalunya 2021 SGR 01581 and European Union NextGenerationEU/PRTR.

References

[1] T.H. Kim, J.S. Park, S.K. Chang, S. Choi, J.H. Ryu, H.K. Song, The current move of lithium ion batteries towards the next phase, Adv. Energy Mater. 2 (2012) 860–872.
[2] J. Zhuang, X. Xu, G. Peleckis, W. Hao, S.X. Dou, Y. Du, Silicene: a promising anode for lithium-ion batteries, Adv. Mater. 29 (2017) 1606716.
[3] F. Duffner, N. Kronemeyer, J. Tübke, J. Leker, M. Winter, R. Schmuch, Post-lithium-ion battery cell production and its compatibility with lithium-ion cell production infrastructure, Nat. Energy 6 (2021) 123–134.
[4] J. Ma, P. Hu, G. Cui, L. Chen, Surface and interface issues in spinel $LiNi_{0.5}Mn_{1.5}O_4$: insights into a potential cathode material for high energy density lithium ion batteries, Chem. Mater. 28 (2016) 3578–3606.
[5] J.W. Choi, D. Aurbach, Promise and reality of post-lithium-ion batteries with high energy densities, Nat. Rev. Mater. 1 (2016) 16013.
[6] Y.M. Zhao, F.S. Yue, S.C. Li, Y. Zhang, Z.R. Tian, Q. Xu, S. Xin, Y.G. Guo, Advances of polymer binders for silicon-based anodes in high energy density lithium-ion batteries, InfoMat 3 (2021) 460–501.
[7] T. Liu, H. Hu, X. Ding, H. Yuan, C. Jin, J. Nai, Y. Liu, Y. Wang, Y. Wan, X. Tao, 12 years roadmap of the sulfur cathode for lithium sulfur batteries (2009–2020), Energy Storage Mater. 30 (2020) 346–366.
[8] Z.L. Xu, S.J. Kim, D. Chang, K.Y. Park, K.S. Dae, K.P. Dao, J.M. Yuk, K. Kang, Visualization of regulated nucleation and growth of lithium sulfides for high energy lithium sulfur batteries, Energy Environ. Sci. 12 (2019) 3144–3155.
[9] D. Yang, Z. Liang, C. Zhang, J.J. Biendicho, M. Botifoll, M.C. Spadaro, Q. Chen, M. Li, A. Ramon, A.O. Moghaddam, J. Llorca, J. Wang, J.R. Morante, J. Arbiol, S. L. Chou, A. Cabot, $NbSe_2$ meets C_2N: A 2D-2D heterostructure catalysts as multifunctional polysulfide mediator in ultra-long-life lithium–sulfur batteries, Adv. Energy Mater. 11 (2021) 2101250.
[10] L. Huang, J. Li, B. Liu, Y. Li, S. Shen, S. Deng, C. Lu, W. Zhang, Y. Xia, G. Pan, X. Wang, Q. Xiong, X. Xia, J. Tu, Electrode design for lithium–sulfur batteries: problems and solutions, Adv. Funct. Mater. 30 (2020) 1910375.
[11] Z.W. Seh, Y. Sun, Q. Zhang, Y. Cui, Designing high-energy lithium-sulfur batteries, Chem. Soc. Rev. 45 (2016) 5605–5634.
[12] D. Yang, Z. Liang, P. Tang, C. Zhang, M. Tang, Q. Li, J.J. Biendicho, J. Li, M. Heggen, R.E. Dunin-Borkowski, M. Xu, J. Llorca, J. Arbiol, J.R. Morante, S. L. Chou, A. Cabot, A high conductivity 1D π–d conjugated metal–organic framework with efficient polysulfide trapping-diffusion-catalysis in lithium–sulfur batteries, Adv. Mater. 34 (2022) 2108835.
[13] X. Wang, Y. Tan, G. Shen, S. Zhang, Recent progress in fluorinated electrolytes for improving the performance of Li–S batteries, J. Energy Chem. 41 (2020) 149–170.
[14] S.E. Cheon, S.S. Choi, J.S. Han, Y.S. Choi, B.H. Jung, H.S. Lim, Capacity fading mechanisms on cycling a high-capacity secondary sulfur cathode, J. Electrochem. Soc. 151 (2004) A2067.
[15] M. Yu, Z. Wang, Y. Wang, Y. Dong, J. Qiu, Freestanding flexible Li_2S paper electrode with high mass and capacity loading for high-energy Li–S batteries, Adv. Energy Mater. 7 (2017) 1700018.
[16] D. Yang, C. Zhang, J.J. Biendicho, X. Han, Z. Liang, R. Du, M. Li, J. Li, J. Arbiol, J. Llorca, Y. Zhou, J.R. Morante, A. Cabot, ZnSe/N-doped carbon nanoreactor with multiple adsorption sites for stable lithium-sulfur batteries, ACS Nano 14 (2020) 15492–15504.
[17] M. Wild, L. O'Neill, T. Zhang, R. Purkayastha, G. Minton, M. Marinescu, G. J. Offer, Lithium sulfur batteries, a mechanistic review, Energy Environ. Sci. 8 (2015) 3477–3494.
[18] Y. He, Y. Qiao, Z. Chang, X. Cao, M. Jia, P. He, H. Zhou, Developing a "polysulfide-phobic" strategy to restrain shuttle effect in lithium–sulfur batteries, Angew. Chem. 131 (2019) 11900–11904.
[19] T. Lei, W. Chen, W. Lv, J. Huang, J. Zhu, J. Chu, C. Yan, C. Wu, Y. Yan, W. He, J. Xiong, Y. Li, C. Yan, J.B. Goodenough, X. Duan, Inhibiting polysulfide shuttling with a graphene composite separator for highly robust lithium-sulfur batteries, Joule 2 (2018) 2091–2104.
[20] X. Chen, T. Hou, K.A. Persson, Q. Zhang, Combining theory and experiment in lithium–sulfur batteries: current progress and future perspectives, Mater. Today 22 (2019) 142–158.
[21] W. Huang, S. Liu, R. Yu, L. Zhou, Z. Liu, L. Mai, Single-atom lithiophilic sites confined within ordered porous carbon for ultrastable lithium metal anodes, Energy Environ. Mater. 6 (2022) e12466.
[22] G. Chen, X. Song, S. Wang, Y. Wang, T. Gao, L.X. Ding, H. Wang, A multifunctional separator modified with cobalt and nitrogen co-doped porous carbon nanofibers for Li–S batteries, J. Memb. Sci. 548 (2018) 247–253.
[23] R. Fang, K. Chen, L. Yin, Z. Sun, F. Li, H.M. Cheng, The regulating role of carbon nanotubes and graphene in lithium-ion and lithium–sulfur batteries, Adv. Mater. 31 (2019) 1800863.
[24] Y. Wang, J. He, Z. Zhang, Z. Liu, C. Huang, Y. Jin, Graphdiyne-modified polyimide separator: a polysulfide-immobilizing net hinders the shuttling of polysulfides in lithium-sulfur battery, ACS Appl. Mater. Interfaces 11 (2019) 35738–35745.
[25] A. Abdul Razzaq, Y. Yao, R. Shah, P. Qi, L. Miao, M. Chen, X. Zhao, Y. Peng, Z. Deng, High-performance lithium sulfur batteries enabled by a synergy between sulfur and carbon nanotubes, Energy Storage Mater. 16 (2019) 194–202.
[26] Y. Hu, W. Chen, T. Lei, Y. Jiao, J. Huang, A. Hu, C. Gong, C. Yan, X. Wang, J. Xiong, Strategies toward high-loading lithium–sulfur battery, Adv. Energy Mater. 10 (2020) 2000082.
[27] Z. Sun, J. Zhang, L. Yin, G. Hu, R. Fang, H.M. Cheng, F. Li, Conductive porous vanadium nitride/graphene composite as chemical anchor of polysulfides for lithium-sulfur batteries, Nat. Commun. 8 (2017) 14627.
[28] Z. Xiao, Z. Yang, L. Wang, H. Nie, M. Zhong, Q. Lai, X. Xu, L. Zhang, S. Huang, A lightweight TiO_2/Graphene interlayer, applied as a highly effective polysulfide absorbent for fast, long-life lithium-sulfur batteries, Adv. Mater. 27 (2015) 2891–2898.
[29] T. Chen, L. Ma, B. Cheng, R. Chen, Y. Hu, G. Zhu, Y. Wang, J. Liang, Z. Tie, J. Liu, Z. Jin, Metallic and polar Co_9S_8 inlaid carbon hollow nanopolyhedra as efficient polysulfide mediator for lithium−sulfur batteries, Nano Energy 38 (2017) 239–248.
[30] C. Zhang, R. Du, J.J. Biendicho, M. Yi, K. Xiao, D. Yang, T. Zhang, X. Wang, J. Arbiol, J. Llorca, Y. Zhou, J.R. Morante, A. Cabot, Tubular CoFeP@CN as a Mott–schottky catalyst with multiple adsorption sites for robust lithium−sulfur batteries, Adv. Energy Mater. 11 (2021) 1–14.
[31] Q. Pang, C.Y. Kwok, D. Kundu, X. Liang, L.F. Nazar, Lightweight metallic MgB_2 mediates polysulfide redox and promises high-energy-density lithium-sulfur batteries, Joule 3 (2019) 136–148.
[32] X. Wang, X. Zhao, C. Ma, Z. Yang, G. Chen, L. Wang, H. Yue, D. Zhang, Z. Sun, Electrospun carbon nanofibers with MnS sulfiphilic sites as efficient polysulfide barriers for high-performance wideerature-range Li-S batteries, J. Mater. Chem. A 8 (2020) 1212–1220.
[33] B. Qiao, A. Wang, X. Yang, L.F. Allard, Z. Jiang, Y. Cui, J. Liu, J. Li, T. Zhang, Single-atom catalysis of CO oxidation using Pt1/FeOx, Nat. Chem. 3 (2011) 634–641.
[34] G. Wang, X. Ke, M. Sui, Advanced TEM characterization for single-atom catalysts: from *ex-situ* towards *in-situ*, Chem. Res. Chin. Univ. 38 (2022) 1172–1184.
[35] R. Chen, J. Zhao, Y. Li, Y. Cui, Y.R. Lu, S.F. Hung, S. Wang, W. Wang, G. Huo, Y. Zhao, W. Liu, J. Wang, H. Xiao, X. Li, Y. Huang, B. Liu, Operando mössbauer spectroscopic tracking the metastable state of atomically dispersed tin in copper oxide for selective CO_2 electroreduction, J. Am. Chem. Soc. (2023), https://doi.org/10.1021/jacs.3c06738.
[36] A. Wang, J. Li, T. Zhang, Heterogeneous single-atom catalysis, Nat. Rev. Chem. 2 (2018) 65–81.
[37] H. Huang, K. Shen, F. Chen, Y. Li, Metal-organic frameworks as a good platform for the fabrication of single-atom catalysts, ACS Catal. 10 (2020) 6579–6586.
[38] L. Jiao, H.L. Jiang, Metal-organic-framework-based single-atom catalysts for energy applications, Chem 5 (2019) 786–804.

[39] Y.Z. Chen, R. Zhang, L. Jiao, H.L. Jiang, Metal–organic framework-derived porous materials for catalysis, Coord. Chem. Rev. 362 (2018) 1–23.

[40] Q. Yang, C.C. Yang, C.H. Lin, H.L. Jiang, Metal–organic-framework-derived hollow n-doped porous carbon with ultrahigh concentrations of single Zn atoms for efficient carbon dioxide conversion, Angew. Chem. Int. Ed. 58 (2019) 3511–3515.

[41] P. Yin, T. Yao, Y. Wu, L. Zheng, Y. Lin, W. Liu, H. Ju, J. Zhu, X. Hong, Z. Deng, G. Zhou, S. Wei, Y. Li, Single cobalt atoms with precise N-coordination as superior oxygen reduction reaction catalysts, Angew. Chem. Int. Ed. 55 (2016) 10800–10805.

[42] H. Tian, H. Tian, S. Wang, S. Chen, F. Zhang, L. Song, H. Liu, J. Liu, G. Wang, High-power lithium–selenium batteries enabled by atomic cobalt electrocatalyst in hollow carbon cathode, Nat. Commun. 11 (2020) 5025.

[43] L. Zhou, P. Zhou, Y. Zhang, B. Liu, P. Gao, S. Guo, 3D star-like atypical hybrid MOF derived single-atom catalyst boosts oxygen reduction catalysis, J. Energy Chem. 55 (2021) 355–360.

[44] Y. Chen, R. Gao, S. Ji, H. Li, K. Tang, P. Jiang, H. Hu, Z. Zhang, H. Hao, Q. Qu, X. Liang, W. Chen, J. Dong, D. Wang, Y. Li, Atomic-Level modulation of electronic density at cobalt single-atom sites derived from metal–organic frameworks: enhanced oxygen reduction performance, Angew. Chem. Int. Ed. 60 (2021) 3212–3221.

[45] Y. Zhang, L. Jiao, W. Yang, C. Xie, H.L. Jiang, Rational fabrication of low-coordinate single-atom Ni electrocatalysts by MOFs for highly selective CO_2 reduction, Angew. Chem. Int. Ed. 60 (2021) 7607–7611.

[46] Q. Shao, L. Xu, D. Guo, Y. Su, J. Chen, Atomic level design of single iron atom embedded mesoporous hollow carbon spheres as multi-effect nanoreactors for advanced lithium-sulfur batteries, J. Mater. Chem. A 8 (2020) 23772–23783.

[47] W.G. Lim, Y. Mun, A. Cho, C. Jo, S. Lee, J.W. Han, J. Lee, Synergistic effect of molecular-type electrocatalysts with ultrahigh pore volume carbon microspheres for lithium-sulfur batteries, ACS Nano 12 (2018) 6013–6022.

[48] S. Ji, Y. Chen, X. Wang, Z. Zhang, D. Wang, Y. Li, Chemical synthesis of single atomic site catalysts, Chem. Rev. 120 (2020) 11900–11955.

[49] H. Zhang, S. Hwang, M. Wang, Z. Feng, S. Karakalos, L. Luo, Z. Qiao, X. Xie, C. Wang, D. Su, Y. Shao, G. Wu, Single atomic iron catalysts for oxygen reduction in acidic media: particle size control and thermal activation, J. Am. Chem. Soc. 139 (2017) 14143–14149.

[50] L. Zhao, Y. Zhang, L.B. Huang, X.Z. Liu, Q.H. Zhang, C. He, Z.Y. Wu, L.J. Zhang, J. Wu, W. Yang, L. Gu, J.S. Hu, L.J. Wan, Cascade anchoring strategy for general mass production of high-loading single-atomic metal-nitrogen catalysts, Nat. Commun. 10 (2019) 1278.

[51] H. Wu, H. Li, X. Zhao, Q. Liu, J. Wang, J. Xiao, S. Xie, R. Si, F. Yang, S. Miao, X. Guo, G. Wang, X. Bao, Highly doped and exposed Cu(I)-N active sites within graphene towards efficient oxygen reduction for zinc-air batteries, Energy Environ. Sci. 9 (2016) 3736–3745.

[52] L. Zhang, D. Liu, Z. Muhammad, F. Wan, W. Xie, Y. Wang, L. Song, Z. Niu, J. Chen, Single nickel atoms on nitrogen-doped graphene enabling enhanced kinetics of lithium–sulfur batteries, Adv. Mater. 31 (2019) 1903955.

[53] J. Zhang, J.Y. Li, W.P. Wang, X.H. Zhang, X.H. Tan, W.G. Chu, Y.G. Guo, Microemulsion assisted assembly of 3D porous S/Graphene@g-C_3N_4 hybrid sponge as free-standing cathodes for high energy density Li–S batteries, Adv. Energy Mater. 8 (2018) 1702839.

[54] C. Lu, Y. Chen, Y. Yang, X. Chen, Single-atom catalytic materials for lean-electrolyte ultrastable lithium-sulfur batteries, Nano Lett. 20 (2020) 5522–5530.

[55] J. Wu, J. Chen, Y. Huang, K. Feng, J. Deng, W. Huang, Y. Wu, J. Zhong, Y. Li, Cobalt atoms dispersed on hierarchical carbon nitride support as the cathode electrocatalyst for high-performance lithium-polysulfide batteries, Sci. Bull. 64 (2019) 1875–1880.

[56] D. Lyu, Y.B. Mollamahale, S. Huang, P. Zhu, X. Zhang, Y. Du, S. Wang, M. Qing, Z. Q. Tian, P.K. Shen, Ultra-high surface area graphitic Fe-N-C nanospheres with single-atom iron sites as highly efficient non-precious metal bifunctional catalysts towards oxygen redox reactions, J. Catal. 368 (2018) 279–290.

[57] Z. Du, X. Chen, W. Hu, C. Chuang, S. Xie, A. Hu, W. Yan, X. Kong, X. Wu, H. Ji, L. J. Wan, Cobalt in nitrogen-doped graphene as single-atom catalyst for high-sulfur content lithium-sulfur batteries, J. Am. Chem. Soc. 141 (2019) 3977–3985.

[58] B.W. Zhang, T. Sheng, Y.D. Liu, Y.X. Wang, L. Zhang, W.H. Lai, L. Wang, J. Yang, Q.F. Gu, S.L. Chou, H.K. Liu, S.X. Dou, Atomic cobalt as an efficient electrocatalyst in sulfur cathodes for superior room-temperature sodium-sulfur batteries, Nat. Commun. 9 (2018) 4082.

[59] H. Tian, A. Song, H. Tian, J. Liu, G. Shao, H. Liu, G. Wang, Single-atom catalysts for high-energy rechargeable batteries, Chem. Sci. 12 (2021) 7656–7676.

[60] L. Zhang, M.N. Banis, X. Sun, Single-atom catalysts by the atomic layer deposition technique, Natl. Sci. Rev. 5 (2018) 628–630.

[61] D. Deng, X. Chen, L. Yu, X. Wu, Q. Liu, Y. Liu, H. Yang, H. Tian, Y. Hu, P. Du, R. Si, J. Wang, X. Cui, H. Li, J. Xiao, T. Xu, J. Deng, F. Yang, P.N. Duchesne, P. Zhang, J. Zhou, L. Sun, J. Li, X. Pan, X. Bao, Chemistry: a single iron site confined in a graphene matrix for the catalytic oxidation of benzene at room temperature, Sci. Adv. 1 (2015) e1500462.

[62] H. Fei, J. Dong, C. Wan, Z. Zhao, X. Xu, Z. Lin, Y. Wang, H. Liu, K. Zang, J. Luo, S. Zhao, W. Hu, W. Yan, I. Shakir, Y. Huang, X. Duan, Microwave-assisted rapid synthesis of graphene-supported single atomic metals, Adv. Mater. 30 (2018) 1802146.

[63] J. Li, Y.f. Jiang, Q. Wang, C.Q. Xu, D. Wu, M.N. Banis, K.R. Adair, K. Doyle-Davis, D.M. Meira, Y.Z. Finfrock, W. Li, L. Zhang, T.K. Sham, R. Li, N. Chen, M. Gu, J. Li, X. Sun, A general strategy for preparing pyrrolic-N_4 type single-atom catalysts via pre-located isolated atoms, Nat. Commun. 12 (2021) 6806.

[64] Z. Liang, D. Yang, P. Tang, C. Zhang, J. Jacas Biendicho, Y. Zhang, J. Llorca, X. Wang, J. Li, M. Heggen, J. David, R.E. Dunin-Borkowski, Y. Zhou, J. R. Morante, A. Cabot, J. Arbiol, Atomically dispersed Fe in a C_2N based catalyst as a sulfur host for efficient lithium–sulfur batteries, Adv. Energy Mater. 11 (2021) 2003507.

[65] S. Karagiannis, G. Chryssolouris, Nd : YAG laser welding — an overview, Proc. SPIE 5131 (2003) 260–264.

[66] S. Rehman, M. Pope, S. Tao, E. McCalla, Evaluating the effectiveness of *in situ* characterization techniques in overcoming mechanistic limitations in lithium–sulfur batteries, Energy Environ. Sci. 15 (2022) 1423–1460.

[67] M. Cuisinier, P.E. Cabelguen, S. Evers, G. He, M. Kolbeck, A. Garsuch, T. Bolin, M. Balasubramanian, L.F. Nazar, Sulfur speciation in Li-S batteries determined by operando X-ray absorption spectroscopy, J. Phys. Chem. Lett. 4 (2013) 3227–3232.

[68] Y. Yan, C. Cheng, L. Zhang, Y. Li, J. Lu, Deciphering the reaction mechanism of lithium–sulfur batteries by *in situ*/operando synchrotron-based characterization techniques, Adv. Energy Mater. 9 (2019) 1900148.

[69] W. Jing, Q. Tan, Y. Duan, K. Zou, X. Dai, Y. Song, M. Shi, J. Sun, Y. Chen, Y. Liu, Defect-rich single atom catalyst enhanced polysulfide conversion kinetics to upgrade performance of Li–S batteries, Small 19 (2023) 2204880.

[70] J. Sun, Y. Sun, M. Pasta, G. Zhou, Y. Li, W. Liu, F. Xiong, Y. Cui, Entrapment of polysulfides by a black-phosphorus-modified separator for lithium–sulfur batteries, Adv. Mater. 28 (2016) 9797–9803.

[71] M. Hagen, P. Schiffels, M. Hammer, S. Dörfler, J. Tübke, M.J. Hoffmann, H. Althues, S. Kaskel, *In-situ* raman investigation of polysulfide formation in Li-S cells, J. Electrochem. Soc. 160 (2013) A1205–A1214.

[72] K. Zhang, Z. Chen, R. Ning, S. Xi, W. Tang, Y. Du, C. Liu, Z. Ren, X. Chi, M. Bai, C. Shen, X. Li, X. Wang, X. Zhao, K. Leng, S.J. Pennycook, H. Li, H. Xu, K.P. Loh, K. Xie, Single-atom coated separator for robust lithium-sulfur batteries, ACS Appl. Mater. Interfaces 11 (2019) 25147–25154.

[73] Q. Wu, Z. Yao, A. Du, H. Wu, M. Huang, J. Xu, F. Cao, C. Li, Oxygen-defect-rich coating with nanoporous texture as both anode host and artificial SEI for dendrite-mitigated lithium–metal batteries, J. Mater. Chem. A 9 (2021) 5606–5618.

[74] Q. Wu, Y. Zheng, X. Guan, J. Xu, F. Cao, C. Li, Dynamical SEI reinforced by open-architecture MOF film with stereoscopic lithiophilic sites for high-performance lithium–metal batteries, Adv. Funct. Mater. 31 (2021) 2101034.

[75] K. Xu, M. Zhu, X. Wu, J. Liang, Y. Liu, T. Zhang, Y. Zhu, Y. Qian, Dendrite-tamed deposition kinetics using single-atom Zn sites for Li metal anode, Energy Storage Mater. 23 (2019) 587–593.

[76] H. Liu, X. Chen, X.B. Cheng, B.Q. Li, R. Zhang, B. Wang, X. Chen, Q. Zhang, Uniform lithium nucleation guided by atomically dispersed lithiophilic CoN_x sites for safe lithium metal batteries, Small Methods 3 (2019) 1800354.

[77] P. Zhai, T. Wang, W. Yang, S. Cui, P. Zhang, A. Nie, Q. Zhang, Y. Gong, Uniform lithium deposition assisted by single-atom doping toward high-performance lithium metal anodes, Adv. Energy Mater. 9 (2019) 1804019.

[78] Y. Sun, J. Zhou, H. Ji, J. Liu, T. Qian, C. Yan, Single-atom iron as lithiophilic site to minimize lithium nucleation overpotential for stable lithium metal full battery, ACS Appl. Mater. Interfaces 11 (2019) 32008–32014.

[79] G. Zhou, E. Paek, G.S. Hwang, A. Manthiram, Long-life Li/polysulphide batteries with high sulphur loading enabled by lightweight three-dimensional nitrogen/sulphur-codoped graphene sponge, Nat. Commun. 6 (2015) 7760.

[80] W. Chen, T. Lei, W. Lv, Y. Hu, Y. Yan, Y. Jiao, W. He, Z. Li, C. Yan, J. Xiong, Atomic interlamellar ion path in high sulfur content lithium-montmorillonite host enables high-rate and stable lithium–sulfur battery, Adv. Mater. 30 (2018) 1804084.

[81] C. Zhu, Q. Shi, S. Feng, D. Du, Y. Lin, Single-atom catalysts for electrochemical water splitting, ACS Energy Lett. 3 (2018) 1713–1721.

[82] M. Li, D. Yang, J.J. Biendicho, X. Han, C. Zhang, K. Liu, J. Diao, J. Li, J. Wang, M. Heggen, R.E. Dunin-Borkowski, J. Wang, G. Henkelman, J.R. Morante, J. Arbiol, S.L. Chou, A. Cabot, Enhanced polysulfide conversion with highly conductive and electrocatalytic iodine-doped bismuth selenide nanosheets in lithium–sulfur batteries, Adv. Funct. Mater. 32 (2022) 2200529.

[83] L. Fang, Z. Feng, L. Cheng, R.E. Winans, T. Li, Design principles of single atoms on carbons for lithium–sulfur batteries, Small Methods 4 (2020) 2000315.

[84] Z. Liang, J. Shen, X. Xu, F. Li, J. Liu, B. Yuan, Y. Yu, M. Zhu, Advances in the development of single-atom catalysts for high-energy-density lithium-sulfur batteries, Adv. Mater. (2022) 2200102.

[85] Y. Li, S. Lin, D. Wang, T. Gao, J. Song, P. Zhou, Z. Xu, Z. Yang, N. Xiao, S. Guo, Single atom array mimic on ultrathin MOF nanosheets boosts the safety and life of lithium–sulfur batteries, Adv. Mater. 32 (2020) 1906722.

[86] J. Wang, B. Ding, X. Lu, H. Nara, Y. Sugahara, Y. Yamauchi, Single atom-based nanoarchitectured electrodes for high-performance lithium–sulfur batteries, Adv. Mater. Interfaces 8 (2021) 2002159.

[87] S. He, J. Yang, S. Liu, X. Wang, X. Che, M. Wang, J. Qiu, Asymmetric N-coordinated iron single-atom catalysts supported on graphitic carbon for polysulfide conversion in lithium-sulfur batteries, Chem. Eng. J. 454 (2023) 140202.

[88] Y. Tao, Y. Wei, Y. Liu, J. Wang, W. Qiao, L. Ling, D. Long, Kinetically-enhanced polysulfide redox reactions by Nb_2O_5 nanocrystals for high-rate lithium-sulfur battery, Energy Environ. Sci. 9 (2016) 3230–3239.

[89] Z. Li, Y. Huang, L. Yuan, Z. Hao, Y. Huang, Status and prospects in sulfur-carbon composites as cathode materials for rechargeable lithium-sulfur batteries, Carbon 92 (2015) 41–63. N. Y.

[90] Q. Xiao, J. Yang, X. Wang, Y. Deng, P. Han, N. Yuan, L. Zhang, M. Feng, C. an Wang, R. Liu, Carbon-based flexible self-supporting cathode for lithium-sulfur batteries: Progress and perspective, 2021.
[91] Q. Wu, Z. Shadike, J. Xu, F. Cao, C. Li, Integrated reactor architecture of conductive network and catalytic nodes to accelerate polysulfide conversion for durable and high-loading Li-S batteries, Energy Storage Mater. 55 (2023) 73–83.
[92] D. Xie, Y. Xu, Y. Wang, X. Pan, E. Härk, Z. Kochovski, A. Eljarrat, J. Müller, C. T. Koch, J. Yuan, Y. Lu, Poly(ionic liquid) nanovesicle-templated carbon nanocapsules functionalized with uniform iron nitride nanoparticles as catalytic sulfur host for Li–S batteries, ACS Nano 16 (2022) 10554–10565.
[93] G. Babu, N. Masurkar, H. Al Salem, L.M.R. Arava, Transition metal dichalcogenide atomic layers for lithium polysulfides electrocatalysis, J. Am. Chem. Soc. 139 (2017) 171–178.
[94] J. He, G. Hartmann, M. Lee, G.S. Hwang, Y. Chen, A. Manthiram, Freestanding 1T MoS_2/graphene heterostructures as a highly efficient electrocatalyst for lithium polysulfides in Li-S batteries, Energy Environ. Sci. 12 (2019) 344–350.
[95] F. Zhou, Z. Li, X. Luo, T. Wu, B. Jiang, L.L. Lu, H. Bin Yao, M. Antonietti, S.H. Yu, Low cost metal carbide nanocrystals as binding and electrocatalytic sites for high performance Li-S batteries, Nano Lett. 18 (2018) 1035–1043.
[96] L. Zhang, Z. Chen, N. Dongfang, M. Li, C. Diao, Q. Wu, X. Chi, P. Jiang, Z. Zhao, L. Dong, R. Che, K.P. Loh, H. Lu, Nickel–cobalt double hydroxide as a multifunctional mediator for ultrahigh-rate and ultralong-life Li–S batteries, Adv. Energy Mater. 8 (2018) 1802431.
[97] Q. Wu, Z. Yao, X. Zhou, J. Xu, F. Cao, C. Li, Built-in catalysis in confined nanoreactors for high-loading Li–S batteries, ACS Nano 14 (2020) 3365–3377.
[98] W. Xia, Y. Chen, W. Wang, Y. Lu, Y. Chen, M. Chen, X. Yang, P. Gao, H. Shu, X. Wang, Enhanced catalytic activity of Co-CoO via VC0.75 heterostructure enables fast redox kinetics of polysulfides in Lithium-Sulfur batteries, Chem. Eng. J. 458 (2023) 141477.
[99] H.J. Li, K. Xi, W. Wang, S. Liu, G.R. Li, X.P. Gao, Quantitatively regulating defects of 2D tungsten selenide to enhance catalytic ability for polysulfide conversion in a lithium sulfur battery, Energy Storage Mater. 45 (2022) 1229–1237.
[100] B. Zhang, J. Wu, J. Gu, S. Li, T. Yan, X.P. Gao, The Fundamental understanding of lithium polysulfides in ether-based electrolyte for lithium-sulfur batteries, ACS Energy Lett. 6 (2021) 537–546.
[101] Q. Liu, X. Han, Q. Dou, P. Xiong, Y. Kang, S.W. Kang, B.K. Kim, H.S. Park, Multiphase and multicomponent nickel-iron oxide heterostructure as an efficient separator modification layer for advanced lithium sulfur batteries, Batter. Supercaps 4 (2021) 1843–1849.
[102] Y. Zhang, J. Liu, J. Wang, Y. Zhao, D. Luo, A. Yu, X. Wang, Z. Chen, Engineering oversaturated Fe-N_5 multifunctional catalytic sites for durable lithium-sulfur batteries, Angew. Chem. Int. Ed. 60 (2021) 26622–26629.
[103] E. Zhang, T. Wang, K. Yu, J. Liu, W. Chen, A. Li, H. Rong, R. Lin, S. Ji, X. Zheng, Y. Wang, L. Zheng, C. Chen, D. Wang, J. Zhang, Y. Li, Bismuth single atoms resulting from transformation of metal–organic frameworks and their use as electrocatalysts for CO_2 reduction, J. Am. Chem. Soc. 141 (2019) 16569–16573.
[104] F. Ma, Y. Wan, X. Wang, X. Wang, J. Liang, Z. Miao, T. Wang, C. Ma, G. Lu, J. Han, Y. Huang, Q. Li, Bifunctional atomically dispersed Mo-N_2/C nanosheets boost lithium sulfide deposition/decomposition for stable lithium-sulfur batteries, ACS Nano 14 (2020) 10115–10126.
[105] X. Fan, S. Chen, W. Gong, X. Meng, Y. Jia, Y. Wang, S. Hong, L. Zheng, L. Zheng, C.W. Bielawski, J. Geng, A conjugated porous polymer complexed with a single-atom cobalt catalyst as an electrocatalytic sulfur host for enhancing cathode reaction kinetics, Energy Storage Mater. 41 (2021) 14–23.
[106] J. Huang, P. Wu, Controlled assembly of luminescent lanthanide-organic frameworks via post-treatment of 3D-printed objects, Nano-Micro Lett. 13 (2021).
[107] Y. Li, G. Chen, J. Mou, Y. Liu, S. Xue, T. Tan, W. Zhong, Q. Deng, T. Li, J. Hu, C. Yang, K. Huang, M. Liu, Cobalt single atoms supported on N-doped carbon as an active and resilient sulfur host for lithium–sulfur batteries, Energy Storage Mater. 28 (2020) 196–204.
[108] Y. Song, W. Zhao, L. Kong, L. Zhang, X. Zhu, Y. Shao, F. Ding, Q. Zhang, J. Sun, Z. Liu, Synchronous immobilization and conversion of polysulfides on a VO_2-VN binary host targeting high sulfur load Li-S batteries, Energy Environ. Sci. 11 (2018) 2620–2630.
[109] Y. Li, J. Wu, B. Zhang, W. Wang, G. Zhang, Z.W. Seh, N. Zhang, J. Sun, L. Huang, J. Jiang, J. Zhou, Y. Sun, Fast conversion and controlled deposition of lithium (poly)sulfides in lithium-sulfur batteries using high-loading cobalt single atoms, Energy Storage Mater. 30 (2020) 250–259.
[110] Y.G. Zhou, S. Zhao, T. Wang, S.Z. Yang, B. Johannessen, H. Chen, C. Liu, Y. Ye, Y. Wu, Y. Peng, C. Liu, S.P. Jiang, Q. Zhang, Y. Cui, Theoretical calculation guided design of single-atom catalysts toward fast kinetic and long-life Li–S batteries, Nano Lett. 20 (2020) 1252–1261.
[111] X. Zhang, T. Yang, Y. Zhang, X. Wang, J. Wang, Y. Li, A. Yu, X. Wang, Z. Chen, Single zinc atom aggregates: synergetic interaction to boost fast polysulfide conversion in lithium-sulfur batteries, Adv. Mater. 35 (2023) 2208470.
[112] S. Zhang, X. Ao, J. Huang, B. Wei, Y. Zhai, D. Zhai, W. Deng, C. Su, D. Wang, Y. Li, Isolated single-atom Ni–N5 catalytic site in hollow porous carbon capsules for efficient lithium–sulfur batteries, Nano Lett. 21 (2021) 9691–9698.
[113] C. Ma, Y. Zhang, Y. Feng, N. Wang, L. Zhou, C. Liang, L. Chen, Y. Lai, X. Ji, C. Yan, W. Wei, Engineering Fe–N coordination structures for fast redox conversion in lithium–sulfur batteries, Adv. Mater. 33 (2021) 2100171.
[114] Z. Han, R. Gao, T. Wang, S. Tao, Y. Jia, Z. Lao, M. Zhang, J. Zhou, C. Li, Z. Piao, X. Zhang, G. Zhou, Machine-learning-assisted design of a binary descriptor to decipher electronic and structural effects on sulfur reduction kinetics, Nat. Catal. 6 (2023) 1073–1086.
[115] Z. Lao, Z. Han, J. Ma, M. Zhang, X. Wu, Y. Jia, R. Gao, Y. Zhu, X. Xiao, K. Yu, G. Zhou, Band structure engineering and orbital orientation control constructing dual active sites for efficient sulfur redox reaction, Adv. Mater. (2023) 2309024.
[116] H. Li, M. Chuai, X. Xiao, Y. Jia, B. Chen, C. Li, Z. Piao, Z. Lao, M. Zhang, R. Gao, B. Zhang, Z. Han, J. Yang, G. Zhou, Regulating the spin state configuration in bimetallic phosphorus trisulfides for promoting sulfur redox kinetics, J. Am. Chem. Soc. 145 (2023) 22516–22526.
[117] Z. Han, S. Zhao, J. Xiao, X. Zhong, J. Sheng, W. Lv, Q. Zhang, G. Zhou, H. M. Cheng, Engineering d-p orbital hybridization in single-atom metal-embedded three-dimensional electrodes for Li–S batteries, Adv. Mater. 33 (2021) 2105947.
[118] Y. Zhang, C. Kang, W. Zhao, Y. Song, J. Zhu, H. Huo, Y. Ma, C. Du, P. Zuo, S. Lou, G. Yin, d-p hybridization-induced "trapping–coupling–conversion" enables high-efficiency Nb single-atom catalysis for Li–S batteries, J. Am. Chem. Soc. 145 (2023) 1728–1739.
[119] L. Ma, J. Qian, Y. Li, Y. Cheng, S. Wang, Z. Wang, C. Peng, K. Wu, J. Xu, I. Manke, C. Yang, P. Adelhelm, R. Chen, Binary metal single atom electrocatalysts with synergistic catalytic activity toward high-rate and high areal-capacity lithium–sulfur batteries, Adv. Funct. Mater. 32 (2022) 2208666.
[120] L. Shen, Y.W. Song, J. Wang, C.X. Zhao, C.X. Bi, S.Y. Sun, X.Q. Zhang, B.Q. Li, Q. Zhang, Synergistic catalysis on dual-atom sites for high-performance lithium–sulfur batteries, Small Struct. 4 (2023) 2200205.
[121] C. Dong, C. Zhou, M. Wu, Y. Yu, K. Yu, K. Yan, C. Shen, J. Gu, M. Yan, C. Sun, L. Mai, X. Xu, Boosting Bi-directional redox of sulfur with dual metal single atom pairs in carbon spheres toward high-rate and long-cycling lithium–sulfur battery, Adv. Energy Mater. 13 (2023) 2301505.
[122] L. Yang, Y. Pan, Z. Zhou, Y. Zhang, J. Xu, C. Ma, Y. Zhang, J. Wang, W. Qiao, L. Ling, Vanadium as auxiliary for Fe–V dual-atom electrocatalyst in lithium–sulfur batteries: "3D in 2D" morphology inducer and coordination structure regulator, ACS Nano 17 (2023) 17405–17416.